LEVEL II (12) NW

Nonlinear Equatorial Spread F: Dependence on Altitude of the F Peak and Bottomside Background Electron Density Gradient Scale Length

S. L. Ossakow, S. T. Zalesak, and B. E. McDonald

Plasma Physics Division
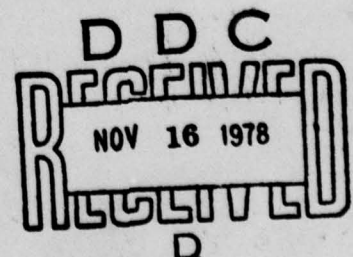
and

P. K. Chaturvedi

University of Maryland
College Park, Maryland 20742

April 1978

DDC
RECEIVED
NOV 16 1978
D

NAVAL RESEARCH LABORATORY
Washington, D.C.

78 11 13 054

NRL-MR-3772

REPORT DOCUMENTATION PAGE		READ INSTRUCTIONS BEFORE COMPLETING FORM
1. REPORT NUMBER NRL Memorandum 3772	2. GOVT ACCESSION NO.	3. RECIPIENT'S CATALOG NUMBER
4. TITLE (and Subtitle) NONLINEAR EQUATORIAL SPREAD F: DEPENDENCE ON ALTITUDE OF THE F PEAK AND BOTTOMSIDE BACKGROUND ELECTRON DENSITY GRADIENT SCALE LENGTH		5. TYPE OF REPORT & PERIOD COVERED Interim report, in a continuing NRL Problem
		6. PERFORMING ORG. REPORT NUMBER
7. AUTHOR(s) S.L. Ossakow, S.T. Zalesak, B.E. McDonald and P.K. Chaturvedi		8. CONTRACT OR GRANT NUMBER(s) X960
9. PERFORMING ORGANIZATION NAME AND ADDRESS Naval Research Laboratory Washington, D.C. 20375		10. PROGRAM ELEMENT, PROJECT, TASK AREA & WORK UNIT NUMBERS NRL Problem #H02-42D; A03-16B. DNA Subtask I25AAXYX960
11. CONTROLLING OFFICE NAME AND ADDRESS Defense Nuclear Agency/Office of Naval Research Washington, D.C. 20305 Arlington, VA 22217		12. REPORT DATE April 1978
		13. NUMBER OF PAGES 64
14. MONITORING AGENCY NAME & ADDRESS(if different from Controlling Office)		15. SECURITY CLASS. (of this report) UNCLASSIFIED
		15a. DECLASSIFICATION/DOWNGRADING SCHEDULE

16. DISTRIBUTION STATEMENT (of this Report)

Approved for public release; distribution unlimited.

17. DISTRIBUTION STATEMENT (of the abstract entered in Block 20, if different from Report)

18. SUPPLEMENTARY NOTES

This research was sponsored in part by the Office of Naval Research and by the Defense Nuclear Agency under Subtask I25AAXYX960; Work Unit Code 11, Title "WB Scintillation Assessment."
*University of Maryland, College Park, MD 20742

19. KEY WORDS (Continue on reverse side if necessary and identify by block number)

Equatorial Spread F, Numerical Simulation, Collisional Rayleigh-Taylor Regime, Parameter dependence

20. ABSTRACT (Continue on reverse side if necessary and identify by block number)

Four different two dimensional (perpendicular to the ambient magnetic field), plasma fluid-type, numerical simulations following the nonlinear evolution of the collisional Rayleigh-Taylor instability in the nighttime equatorial F region ionosphere have been performed. Realistic altitude dependent ion-neutral collision frequencies, recombination rates, and ambient electron density profiles were used. In three cases (ESF 0, 1, 3) the electron density profile was kept constant, with a minimum bottomside background electron density gradient scale length $L \sim 10$ km, but the altitude of the F peak was changed, with F peak altitudes at 340, 350, and 430 km. All cases resulted in bottomside growth of the instability (Spread F) with dramatically different time scales

DD FORM 1473 (1 JAN 73)   EDITION OF 1 NOV 65 IS OBSOLETE
S/N 0102-014-6601

for development. Plasma density depletions were produced on the bottomside with rise velocities, produced by nonlinear polarization $E \times B$ forces, of 2.5, 12, and 160 m/sec, and percentage depletions of 16, 40, and 85, respectively. In one case, ESF 0, the bubble did not rise to the topside, but in ESF 1 and 3 topside irregularities were produced by the bubbles (where linear theory predicts no irregularities.) In these three cases Spread F could be described from weak to strong. In the fourth case (ESF 2) the altitude of the F peak was 350 km, but the minimum L on the bottomside was changed to 5 km. This resulted in a bubble rise velocity $\sim$ 23 m/sec and a 60% depletion with strong bottomside and moderate topside Spread F and a time scale for development between ESF 1 and 3. Two other cases ESF 0' and 0″ with peaks at 330 and 300 km, respectively and bottomside L $\sim$ 10 km were investigated via linear theory. These cases resulted in extremely weak bottomside Spread F and no Spread F (entire bottomside linearly stable), respectively. These simulations show that, under appropriate conditions, the collisional Rayleigh-Taylor instability causes linear growth on the bottomside of the F region. This causes the formulation of plasma density depletions (bubbles) which rise to the topside (under appropriate conditions) F region by polarization $E \times B$ motion. High altitude of the F peak, small bottomside electron density gradient scale lengths, and large percentage depletions yield large vertical bubble rise velocities, with the first two conditions favoring bottomside linear growth of the instability. The numerical simulation results are in good agreement with rocket and satellite in situ measurements and radar backscatter measurements, including some of the recent results from the August 1977 coordinated ground based measurement campaign conducted by DNA at Kwajalein.

LEVEL II

ACCESSION for

NTIS   White Section
DDC   Buff Section □
UNANNOUNCED □
JUSTIFICATION

BY
DISTRIBUTION/AVAILABILITY CODES

Dist.   AVAIL. and/or SPECIAL

A

D D C
RECEIVED
NOV 16 1978
D

CONTENTS

NONLINEAR EQUATORIAL SPREAD F:
DEPENDENCE ON ALTITUDE OF THE F PEAK
AND BOTTOMSIDE BACKGROUND ELECTRON
DENSITY GRADIENT SCALE LENGTH

I. INTRODUCTION

In the past few years much effort has been expended to describe and explain equatorial

Spread F phenomena both from an experimental and theoretical viewpoint (see for example:

Balsley et al., 1972; *Haerendel*, 1974; *Dyson et al.*, 1974; *Chaturvedi and Kaw*, 1975a,b,; 1976;

Hudson and Kennel, 1975; *Scannapieco and Ossakow*, 1976; *Kelley et al.*, 1976; *Woodman and La*

Hoz, 1976; *Morse et al.*, 1977; *McClure et al.*, 1977; *Chaturvedi and Ossakow*, 1977; *Zalesak et*

al., 1977; *Szuszczewicz*, 1978; *Ott*, 1978; *Ossakow and Chaturvedi*, 1978; *Ossakow et al.*, 1978;

Hudson, 1978; *Costa and Kelley*, 1978a,b; and *Kelley and Ott*, 1978). It is now generally believed

that the collisional Rayleigh-Taylor instability (or possibly the $E \times B$ gradient drift instability;

in any case a fluid type gradient instability) initiates equatorial Spread F in the bottomside

evening equatorial F region ionosphere (*Balsley et al.*, 1972; *Haerendel*, 1974; *Scannapieco and*

Ossakow, 1976). Several recent experimental results lend credence to this idea (*Kelley et al.*,

1976; *Woodman and La Hoz*, 1976; *McClure et al.*, 1977). The generation of this instability on

the bottomside leads to the formation of plasma density depletions (bubbles). These bubbles

were predicted by the nonlinear numerical simulation studies (in the collisional Rayleigh-

Taylor regime, denoted CR-T) of *Scannapieco and Ossakow* [1976] and have been observed ex-

perimentally (*Kelley et al.*, 1976; *Woodman and La Hoz*, 1976; *McClure et al.*, 1977).

The initial nonlinear numerical simulation studies (*Scannapieco and Ossakow*, 1976)

showed how a plasma mode (CR-T), which is linearly unstable on the bottomside only, could,

by nonlinear polarization $\mathbf{E} \times \mathbf{B}$ forces in the equatorial geometry, produce bubble induced irregularities on the topside, where the mode is linearly stable. In the present paper we give a more comprehensive derivation of the equations used by *Scannapieco and Ossakow* (1976) and extend the simulations in the CR-T regime by changing background ionospheric parameters. In particular, the altitude of the *F* peak is changed in different simulations, as is the bottomside background electron density gradient scale length. Both of these changes lead to important new simulation results. However, the most profound effect comes from changing the height of the *F* peak as this changes the effective ion-neutral collision frequency.

In section II the theory is presented; section III contains the numerical simulation results and discussion; and section IV gives the summary and conclusions.

II. THEORY

In this section we present the two dimensional (x, y; see Fig. 1) set of plasma fluid equations which are used to describe the nonlinear evolution of the collisional Rayleigh-Taylor (CR-T) instability for equatorial nighttime *F* region conditions. The ambient geomagnetic field, $\mathbf{B}$, is taken to be constant and in the z direction, the y axis is vertically upward (altitude), gravity, $\mathbf{g}$, is in the negative y direction, the x axis points westward, and $\mathbf{g} \times \mathbf{B}$ is toward the east. The ambient electron density profile depicted in Fig. 1 shows a steep bottomside. The bottomside steepens due to recombination effects and electrodynamic forces. In what follows we will neglect any motions or variations parallel to $\mathbf{B}$. Consequently, all spatial derivatives will be taken in the x, y plane. The basic plasma two-fluid equations describing the system are

$$\frac{\partial n_\alpha}{\partial t} + \nabla \cdot (n_\alpha \mathbf{v}_\alpha) = -\nu_R (n_\alpha - n_{\alpha 0})$$

$$\left(\frac{\partial}{\partial t} + \mathbf{v}_\alpha \cdot \nabla \right) \mathbf{v}_\alpha = \frac{q_\alpha}{m_\alpha} \left(\mathbf{E} + \frac{\mathbf{v}_\alpha \times \mathbf{B}}{c} \right) + \mathbf{g} - \nu_\alpha \mathbf{v}_\alpha$$

where the subscript α denotes species (e is electron, i is ion), n is charged particle number den-

sity, $\mathbf{v}$ is velocity; ν_R is recombination rate; $\mathbf{E}$ is the electric field; $\mathbf{g}$ is gravity; q is the charge, ν is collision frequency; c is the speed of light; and m is mass.

It should be noted that $n_{\alpha o}$ in Eq. (1) is the equilibrium value of the density such that in equilibrium the right hand side of Eq. (1) is zero. In the usual form the right hand side of Eq. (1) would have a source minus a loss. The loss term is represented by $-\nu_R n_\alpha$ (*Strobel and McElroy*, 1970) and we have set the source term equal to $\nu_R n_{\alpha o}$ such that $dn_{\alpha o}/dt = 0$. The recombination rate, ν_R, represents a combination of the rate limiting charge exchange reaction

$$O^+ + O_2 \xrightarrow{K_1} O_2^+ + O$$

(3)

and the ion-molecule reaction

$$O^+ + N_2 \xrightarrow{K_2} NO^+ + N$$

(4)

such that

$$\nu_R = K_1 n(O_2) + K_2 n(N_2)$$

(5)

where $n(O_2)$ and $n(N_2)$ are the neutral number densities of O_2 and N_2 respectively. In Eq. (2) the temperature and neutral wind have been set to zero (equivalently we are in a frame moving with the neutral wind).

Equation (2) is then solved for the electron and ion velocities as follows. The left hand side of Eq. (2), i.e., the inertial terms, are neglected so that the time changes associated with these terms occur over a time scale longer than the gyroperiod or collision time (equivalently the frequency associated with the inertial terms is small compared to the gyrofrequencies and collision frequencies). For the electrons we take $\nu_e/\Omega_e = 0$, where $\Omega_\alpha = eB/m_\alpha c$ and for the ions $\nu_i/\Omega_i \ll 1$, where by ν_i we mean ion-neutral collisions (ν_{in}). The equations for the electron and ion velocities are then given by

3

$$\mathbf{v}_e = \frac{c}{B}\,\mathbf{E} \times \hat{z}, \quad \hat{z} = \frac{\mathbf{B}}{|\mathbf{B}|}$$

(6)

$$\mathbf{v}_i = \left(\frac{\mathbf{g}}{\Omega_i} + \frac{c}{B}\,\mathbf{E}\right) \times \hat{z} + \left(\frac{\mathbf{g}}{\Omega_i} + \frac{c}{B}\,\mathbf{E}\right)\frac{\nu_{in}}{\Omega_i}$$

(7)

where in (6) we have neglected the electron $\mathbf{g} \times \hat{z}$ motion, because compared with the same ion motion the ratio is m_e/m_i. Use is made of quasi-neutrality such that $n_e = n_i = n$ and we use

$$\nabla \cdot \mathbf{j} = 0, \quad \mathbf{j} = en(\mathbf{v}_i - \mathbf{v}_e)$$

(8)

Eq. (8) can be obtained by subtracting the electron continuity equation from the ion continuity equation (Eq. (1) in the appropriate forms). The electrostatic approximation is made, i.e., $\mathbf{E} = -\nabla\phi$ and we then obtain

$$\frac{\partial n}{\partial t} - \frac{c}{B}(\nabla\phi \times \hat{z}) \cdot \nabla n = -\nu_R(n - n_o)$$

(9)

$$\nabla \cdot (\nu_{in}n\nabla\phi) = \frac{m_i}{e}\,\mathbf{g} \cdot \nabla(\nu_{in}n) + \frac{B}{c}(\mathbf{g} \times \hat{z}) \cdot \nabla n$$

(10)

Then we set $\phi = \phi_o + \phi_1$, where ϕ_o is the zero order potential and ϕ_1 is the induced or perturbed potential. The zero order solution of Eqs. (9) and (10) requires that $\nabla\phi_o = m_i\mathbf{g}/e$. Note that this equilibrium value of the potential makes $\mathbf{v}_{io} = 0$ (see Eq. (7)) and makes $\mathbf{v}_{eo} = -(\mathbf{g} \times \hat{z}/\Omega_i)$. Thus the equilibrium current is carried by the electrons and we have $\mathbf{j}_o = -n_o e\mathbf{g}\hat{x}/\Omega_i$. We then neglect any other zero order or ambient electric fields so that Eqs. (9) and (10) become

$$\frac{\partial n}{\partial t} - \frac{c}{B}(\nabla\phi_1 \times \hat{z}) \cdot \nabla n = -\nu_R(n - n_o)$$

(11)

$$\nabla \cdot (\nu_{in}n\nabla\phi_1) = \frac{B}{c}(\mathbf{g} \times \hat{z}) \cdot \nabla n$$

(12)

4

If ν_{in} were constant then $(B/c\nu_{in})$ $(g \times \hat{z})$ would play the role of an effective electric field (see *Ossakow and Chaturvedi*, 1978) and $-\nabla\phi_1$ is the induced or polarization electric field. Equations (11) and (12) are the basic equations we wish to solve for n and ϕ_1 in the x, y plane. In these equations n_o, ν_{in}, and ν_R are functions of y (altitude).

We may obtain the linear growth rate from Eqs. (11) and (12) by assuming that

$$n = n_o(y) + n_1 e^{i(k_x x + k_y y - \omega t)}$$

$$\phi_1 = \phi_1 e^{i(k_x x + k_y y - \omega t)}$$

$$(13)$$

where we have made the local approximation $k \gg (\partial n_o/\partial y)$ $(1/n_o)$. This results in the determinant set of equations

$$(-i\omega + \nu_R)n_1 + i\frac{c}{B}\frac{\partial n_o}{\partial y} k_x \phi_1 = 0$$

$$(14)$$

$$\frac{B}{c} i k_x g n_1 + \left[\frac{\partial(n_o \nu_{in})}{\partial y} i k_y - n_o \nu_{in} k^2\right]\phi_1 = 0$$

$$(15)$$

This set yields

$$\omega = -\frac{i k_x^2 g \dfrac{\partial n_o}{\partial y}}{i k_y \dfrac{\partial(n_o \nu_{in})}{\partial y} - n_o \nu_{in} k^2} - i\nu_R$$

$$(16)$$

Setting $\omega = \omega_r + i\gamma$ we obtain

$$\gamma = \frac{\dfrac{\partial n_o}{\partial y} k_x^2 g n_o \nu_{in} k^2}{(n_o \nu_{in} k^2)^2 + \left[k_y \dfrac{\partial(n_o \nu_{in})}{\partial y}\right]^2} - \nu_R$$

$$(17)$$

$$\omega_r = \frac{-k_x^2 k_y \dfrac{\partial(n_o \nu_{in})}{\partial y} g \dfrac{\partial n_o}{\partial y}}{(n_o \nu_{in} k^2)^2 + \left[k_y \dfrac{\partial(n_o \nu_{in})}{\partial y}\right]^2}$$

$$(18)$$

5

Equation (17) for the growth rate, γ, clearly shows that one can have growth (positive γ) only on the bottomside of the F peak where $\partial n_o/\partial y > 0$. Moreover, growth (instability) occurs when the first term in (17) is greater than the second. Equation (17) clearly shows that on the topside where $\partial n_o/\partial y < 0$ γ is negative (stable). For purely horizontal propagating waves ($k_y - 0$) the above discussion still applies and we obtain

$$\gamma = \frac{1}{n_o} \frac{\partial n_o}{\partial y} \frac{g}{\nu_{in}} - \nu_R \tag{19}$$

$$\omega_r = 0 \tag{20}$$

and we can identify $n_o(\partial n_o/\partial y)^{-1}$ with the background electron density gradient scale length L. In the denominator of Eqs. (17) and (18) the second term is small compared with the first if $kL \gg 1$ (neglecting the ν_{in} altitude dependence) which is just the local approximation. Then Eqs. (17) and (18) become

$$\gamma = \frac{1}{n_o} \frac{\partial n_o}{\partial y} \frac{k_x^2}{k^2} \frac{g}{\nu_{in}} - \nu_R \tag{21}$$

$$\omega_r = - \frac{k_x^2 k_y g \dfrac{\partial n_o}{\partial y} \dfrac{\partial(n_o \nu_{in})}{\partial y}}{(n_o \nu_{in} k^2)^2} \tag{22}$$

Equation (21) shows that the growth rate is independent of $|k|$ and maximizes when $k^2 = k_x^2$ (horizontal propagation). Also if one neglects the y dependence of ν_{in} then (22) shows that $\omega_r \sim - (g/\nu_{in}L)(1/kL)$ or $-(kL)^{-1}$ times the growth rate.

III. NUMERICAL RESULTS AND DISCUSSION

The basic equations to be solved are (11) and (12). Equation (11) is put into dimensionless form with $Q \equiv n/n_o$. Equation (11) then becomes

6

$$\frac{\partial Q}{\partial t} - \frac{c}{B}\left[\frac{\partial}{\partial x}\left(Q\frac{\partial}{\partial y}\phi_1\right) - \frac{\partial}{\partial y}\left(Q\frac{\partial}{\partial x}\phi_1\right)\right]$$

$$= -\frac{c}{B}\frac{Q}{n_o}\frac{\partial n_o}{\partial y}\frac{\partial\phi_1}{\partial x} - \nu_R(Q-1) \tag{23}$$

where we have used $\partial n_o/\partial t = 0$. Equation (12) becomes

$$\frac{\partial^2\phi_1}{\partial x^2} + \frac{\partial^2\phi_1}{\partial y^2} + \left\{\frac{1}{\nu_{in}}\frac{\partial\nu_{in}}{\partial y} + \frac{1}{Q}\frac{\partial Q}{\partial y} + \frac{1}{n_o}\frac{\partial n_o}{\partial y}\right\}\frac{\partial\phi_1}{\partial y}$$

$$+ \frac{1}{Q}\frac{\partial Q}{\partial x}\frac{\partial\phi_1}{\partial x} = -\frac{B}{c}\frac{g}{\nu_{in}}\frac{1}{Q}\frac{\partial Q}{\partial x}. \tag{24}$$

In Eqs. (23) and (24) ν_{in} and ν_R are functions of altitude (y). The ion-neutral collision frequency, ν_{in}, is given by (*Strobel and McElroy*, 1970)

$$\nu_{in} = 2.4 \times 10^{-11}\sqrt{T}\,n_n \tag{25}$$

where n_n is the neutral density in cm^{-3}, and T is the atmospheric temperature in °K. Equation (25) represents the collision frequency for 0^+ in 0. The recombination rate, ν_R, is given by Eq. (5) with (*McFarland et al.*, 1973)

$$K_1 = 2 \times 10^{-11}\left(\frac{300}{T}\right)^{0.4} \tag{26}$$

$$K_2 = \begin{cases} 1.2 \times 10^{-12}\left(\dfrac{300}{T}\right), & T \leqslant 750°K \\[2ex] 8 \times 10^{-14}\left(\dfrac{T}{300}\right)^2, & T > 750°K \end{cases} \tag{27}$$

The atmospheric quantities in Eqs. (5), (25), (26) and (27) were obtained from a Jacchia 1965 model neutral atmosphere. Both ν_{in} and ν_R used in the numerical simulations are depicted in Fig. 2.

7

The results of four nonlinear numerical simulations will be presented. The simulations are listed in Table 1 and the differences in the ambient zero order driving conditions are clearly delineated. For these equatorial spread F (ESF) cases only those parameters listed in the table were changed. All other conditions were the same from simulation to simulation. ESF 1 is taken to be the canonical case because it has essentially the original simulation conditions of *Scannapieco and Ossakow* (1976). In ESF O we have taken the $n_o(y)$ profile of ESF 1 and moved it down 10 km, i.e., the shape is the same but the n_o at any altitude changes (see Figs. 5 and 11). Similarly in ESF 3 the profile of ESF 1 is moved up 80 km (see Figs. 5 and 9). In ESF 2 in the region of maximum growth rate of ESF 1 the bottomside ambient electron density gradient scale length has been made smaller, i.e., the bottomside profile is steeper, (see Figs. 5 and 7). The linear growth rates for these four cases are plotted in Fig. 3. For completeness, linear damping rates for two other cases ESF O' and ESF O" are displayed in Fig. 4. ESF O' is the same profile as ESF 1 with the F peak moved down 20 km. ESF O" is also the same profile as ESF 1, but with the peak moved down 50 km. In arriving at the curves in Figs. 3 and 4, a horizontal perturbation was assumed, i.e., $n_1, \phi_1 \propto \exp[i(k_x x - \omega t)]$ and use was made of Eq. (19) with ν_{in} and ν_R as given in Fig. 2.

All four nonlinear numerical simulations were performed over a two dimensional mesh corresponding to an altitude (y) range of 200 km, i.e., the highest y point minus the lowest y point was 200 km, and an east-west (x) extent of 8 km (see Figs. 5, 7, 9 and 11). The mesh was such that there were 102 points in the y direction and 42 points in the x direction and periodic boundary conditions in both directions. This corresponds to $\Delta y = 2$ km and $\Delta x = 200$ meters. Equation (23) was integrated forward in time using flux-corrected transport algorithms (*Boris and Book*, 1973), while Eq. (24) was solved using a Chebychev-iterative relaxation technique (*McDonald*, 1977). The background zero order ionospheric electron density, n_o, em-

8

ployed in each simulation is depicted in Figs. 5, 7, 9 and 11. Superimposed on the background density at $t = 0$ was an initial cosinelike perturbation (the same for each simulation) of the form (applied over the entire mesh),

$$\frac{n_1}{n_o} = Q - 1 = -e^{-3} \begin{cases} \cos\left(\frac{\pi x}{1.6}\right), & 0 \leqslant |x| \leqslant 1.6 \; km \\ \frac{1}{2}\left[\cos\left(\frac{\pi x}{1.6}\right) - 1\right], & 1.6 \leqslant |x| \leqslant 3.2 \; km \\ 0, & |x| > 3.2 \; km \end{cases} \tag{28}$$

where x is in km and $x = 0$ is in the center of the x mesh (see Figs. 5, 7, 9 and 11).

ESF 1 Case. The n_o profile used in this canonical case is depicted in Fig. 5. The y extent of the mesh runs from 252 km to 452 km with the F peak at 354 km. The shortest bottomside background electron density gradient scale lengths $L = n_o (\partial n_o / \partial y)^{-1}$ are ~ 10 km and essentially occur in the range 252 to 298 km. The largest linear growth rate (see Fig. 3), $\gamma_M = 1.01 \times 10^{-3}$ sec^{-1} and occurs at an altitude of 298 km. At this altitude $\nu_R = 3.7 \times 10^{-4}$ sec^{-1}. Figure 3 depicts the range of linear instability for ESF 1 and this is from 274 to 350 km in altitude. Below 274 km L is small, but recombination prevails (see Fig. 2) and between 350 and 354 L is large and recombination prevails. Exactly at the F peak (354 km), $\partial n_o / \partial y = 0$, i.e., $L = \infty$, and $\gamma = -\nu_R$ (see Eq. (19)). Of course above 354 km (the F peak in this case), the gradient changes sign and all perturbations are linearly stable. Note in Fig. 3 that for all cases we have plotted only the regions of instability (growth), i.e., positive γ. Between 274 km and 298 km γ goes from 4.4×10^{-5} sec^{-1} to 1.01×10^{-3} sec^{-1} and ν_R goes from 7.98×10^{-4} to 3.73×10^{-4} sec^{-1}. Between 298 km and 350 km, γ goes from 1.01×10^{-3} sec^{-1} to 3.48×10^{-5} sec^{-1} and ν_R at 350 km is 7.47×10^{-5} sec^{-1}.

9

Figure 5 exhibits contour plots of constant n/n_0 or equivalently n_1/n_0, at $t = 2000$, 4000, 8000, and 10,000 sec in the development of ESF 1. Each is overlayed with a plot of n_0 (large dashed curve) as a function of altitude. At $t = 2000$ sec the early phase of the growth of the collisional Rayleigh-Taylor instability is exhibited. It shows the formation of plasma density enhancements (+) and depletions ($-$), depicted by small dashed and solid contours, respectively. The depletion contour represents a 16% depletion, with a maximum depletion of 27% within this contour; whereas, the enhancement contour represents a 19% enhancement, with a maximum enhancement of 23% within this contour. Here and in subsequent Figures 7, 9, and 11 the contour plotting is such that the first (outer) depletion contour n/n_0 is $2^{-1/4}$ and each succeeding inner contour is $2^{-1/2}$ times the previous one. Then we subtract 1.0 to find n_1/n_0 for depletions. For example, for three depletion contours, the outermost would have $n_1/n_0 = 0.84$ (16% depletion), the next inner one $n_1/n_0 = 0.59$ (41% depletion), and the innermost $n_1/n_0 = 0.42$ (58% depletion). For the enhancement contours, the first outer contour is $2^{1/4}$ and the succeeding inner ones are $2^{1/2}$ times the previous ones. Then, we subtract 1.0 to obtain n_1/n_0 for enhancements. For example, for three enhancement contours, the outermost would have $n_1/n_0 = 1.19$ (19% enhancement), the next inner one $n_1/n_0 = 1.68$ (68% enhancement), and the innermost $n_1/n_0 = 2.38$ (138% enhancement). With this scheme, for the depletions (enhancements) every other contour of n_1/n_0 is a factor of two smaller (larger).

At $t = 4,000$ sec, in Fig. 5. a clear bubble (density depletion) in the center of the x direction is beginning to form and rise toward the F peak with an innermost depletion contour of 41% with a maximum depletion within this contour of 54%. The innermost enhancement contour is 68%, with a maximum enhancement of 84% within this contour. We also note the formation of other depletions in the wings (near $|x| \sim 4$ km). At $t = 8000$ sec, the density depletion or bubble upper boundary is at the F peak. The innermost contour of the rising bubble is a 41% depletion; however, there is a 58% depletion contour below this at an altitude ~ 300 km and within this contour a maximum depletion of 66%. In the wings there are depletions with

10

innermost contours of 71% depletion. There are plasma density enhancements at $y \leqslant 302$ km
with innermost contours of 138% enhancements and maximum enhancements inside these in-
nermost contours of 226%.

At $t = 10,000$ sec (as far as the ESF 1 simulation was carried), the main bubble is clearly
through the F peak with an innermost depletion contour of 41%. However, in the ionosphere
below the bubble near $x = 0$, there is a 71% depletion contour with a maximum depletion in-
side this contour of 73%. In the wings there are depletions with innermost contours of 71%
and inside of these depletion contours maximum depletions of 75%. The innermost enhance-
ment contour is 236% with a maximum inside this contour of 294%.

Although there is a main bubble which is beyond the F peak (top of bubble at 375 km)
at this time, it has not completely broken from the lower altitude region and is forming a trail-
ing tail. The top of the main bubble in the central x region is at an altitude ~ 375 km with
the bottom of the trail at an altitude ~ 270 km. The widest part of the top outermost contour
(16% depletion) of the bubble is ~ 3 km, whereas; the innermost contour (41% depletion) is
~ 0.5 km wide. Also from $t = 8,000$ to $t = 10^4$ sec in Fig. 5, the top most part of the bubble
has moved ~ 24 km which corresponds to a rise velocity ~ 12 m/sec. At this time the
enhanced regions encompass a large region in the east-west (x) direction although confined in
altitudes $\leqslant 320$ km (basically isolated depletions move upward, while isolated enhancements
move downward in the equatorial spread F geometry; see *Ossakow and Chaturvedi*, 1978).

Figure 6 displays contours of constant induced potential ϕ_1, from Eq. (24), for ESF 1
over the computational mesh at $t = 10^4$ sec. The plus (inside solid lines) denotes positive
values and the minus (inside dashed lines) denotes negative values of potential. Zero potential
falls between the two in such a way that the outermost solid contour represents a potential of
5×10^{-4} statvolts (0.15 volts) and the outermost dashed contour represents a potential of

11

-5×10^{-4} statvolts. Each inner solid contour represents an increment of 5×10^{-4} statvolts and similarly each inner dashed contour represents an increment of -5×10^{-4} statvolts. Consequently, the potential difference between any two solid (dashed) contours is 5×10^{-4} (-5×10^{-4}) statvolts. However, the potential difference between the outermost solid and dashed contours is 10^{-3} statvolts (0.3 volts). This contour level scheme is the same in Figs. 8 and 10. We see that the more isolated high altitude part of the central bubble is acted on by an induced electric field which points from west (positive x) to east (negative x) and is dipolar in nature. This causes the bubble to rise with a velocity $(-c/B)\nabla \phi_1 \times \hat{z}$. However, the lower portion of the mesh is acted on by an induced electric field which points from east to west and is much weaker than the induced electric field acting upon the isolated portion of the central bubble. This basically causes the enhancements to move downward along with the lower altitude depletions. Thus the lower part of the central bubble becomes "captured" by the enhancements. As stated previously isolated depletions and enhancements should move up and down respectively, at the equator. However, this concept is altered when depletions are surrounded by enhancements or vice versa.

ESF 2 Case. The n_o profile used in this case is displayed in Fig. 7. The y extent is the same as ESF 1 with the F peak at 354 km. However, in this case the bottomside is steeper than ESF 1 and the shortest bottomside background electron density gradient scale lengths L are ~ 4.8 km and occur in the altitude range between 296 and 304 km. The largest linear growth rate (see Fig. 3), $\gamma_M = 3.2 \times 10^{-3}$ sec^{-1} (a factor of three larger than ESF 1) and occurs at an altitude of 304 km. At this altitude $\nu_R = 3.09 \times 10^{-4}$ sec^{-1}. The range of linear instability for ESF 2 is depicted in Fig. 3. This goes from 282 km to 352 km in altitude. At the lowest altitudes n_o is approximately the same for ESF 1 and 2. This makes L larger at lower altitudes for ESF 2. Consequently, while ESF 1 is linearly unstable down to an altitude of

274 km, ESF 2 is unstable only down to 282 km. Between 282 and 304 km γ goes from 4.5 $\times$ 10 $^{-5}$ sec $^{-1}$ to 3.2 $\times$ 10 $^{-3}$ sec $^{-1}$ and ν_R goes from 6.19 $\times$ 10 $^{-4}$ sec $^{-1}$ to 3.09 $\times$ 10 $^{-4}$ sec $^{-1}$. Between 306 km and 352 km, γ goes from 2 $\times$ 10 $^{-3}$ sec $^{-1}$ to 6.82 $\times$ 10 $^{-5}$ sec $^{-1}$ and ν_R at 352 km is 7.02 $\times$ 10 $^{-5}$ sec $^{-1}$.

Figure 7 shows contour plots of constant n/n_o (or n_1/n_o) at $t = 1000$, 3000, 4000, and 5000 sec in the nonlinear development of ESF 2. Also depicted in each snapshot in this figure is a plot of n_o as a function of altitude for this simulation. At $t = 1000$ sec the innermost depletion contour represents a 58% depletion with a maximum depletion inside this contour of 60%. The enhancement contour represents a 19% enhancement. However, because of the enhancement contour spacings, there exists a 63% maximum enhancement inside the enhancement contour. This first frame clearly shows that ESF 2 is developing faster than ESF 1. At $t = 3000$ sec the bubble is clearly rising toward the F peak. In the upper part of the bubble, near 340 km, the innermost depletion contour represents a 71% depletion. However, a maximum depletion of 82% occurs in the lower portion of the bubble, near 315 km, inside the 79% depletion contour. At this time the enhancement contours are much more widespread than in the case of ESF 1 with a maximum enhancement of 2490%. These enhancements are confined in altitude with 280 km $\leqslant y \leqslant$ 305 km. At $t = 4000$ sec the main part of the bubble is already past the peak. In the upper part of the bubble the innermost depletion contour is 58%; however, a maximum depletion of 68% occurs inside the third (innermost) depletion contour at lower ($\sim$ 320 km) altitudes, i.e., within the trail. Some well defined depletions (bubbles) are also evident in the lower regions ($\sim$ 310 km altitude) to the east and west of the main bubble ($|x| \sim 2$ km). Also at this time there are large regions of enhancements confined to altitudes 275 km $\leqslant y \leqslant$ 310 km with maximum enhancements of 2936%.

At $t = 5000$ sec (as far as ESF 2 was run), the bubble clearly is well past the F peak leaving a trail in the lower ionosphere. However, the trail is not as well captured as in ESF 1. The

13

bubble and trail here extend for about 100 km in altitude as was the case in ESF 1. The inner-most contour of the high altitude part of the bubble (top of bubble at 387 km altitude) is now only 41% and there is a maximum depletion of 73% in the lower portion of the bubble, near 325 km, within the 71% depletion contour. The widest part of the 16% depletion contour near the top of the bubble is $\sim$ 3 km; whereas, the 41% depletion (inner) contour is $\sim$ 0.5 km wide. Between $t = 3000$ and 4000 sec the top of the bubble has moved up $\sim$ 23 km which corresponds to a rise velocity $\sim$ 23 m/sec. There is a slight rise in the bubbles to the east and west of the main bubble (compare with $t = 4000$ sec). The enhancements are confined between 275 km $\leqslant y \leqslant$ 310 km with a maximum enhancement of 3130%.

Figure 8 depicts contours of constant induced potential ϕ_1 for ESF 2 over the computational mesh at $t = 5000$ sec. The contours have the same scheme as for ESF 1. Once again this figure shows that the more isolated high altitude part of the bubble is acted upon by an induced polarization electric field which points from west to east and is somewhat dipolar in nature. This field is stronger than in the case of ESF 1 (see Fig. 6; note that in ESF 2 there are more potential contours and the spacing between the outermost negative contour and outermost positive contour is closer for ESF 2 than ESF 1) and accounts for the more rapid rise (through $-(c/B) \nabla\phi_1 \times \hat{z}$). The lower portion of the mesh, like ESF 1, is acted upon by an induced electric field which points from east to west and is much weaker than the induced electric field which acts on the isolated portion of the central bubble. This field keeps the lower portion containing enhancements and depletions at low altitudes.

ESF 3 Case. Displayed in Fig. 9 is the n_o profile used in this case. The y extent is now between 332 km and 532 km with the F peak at 434 km. This F peak is 80 km higher than ESF 1 and is about at the altitude that *Kelley et al.* [1976] measured the F peak after encountering a bubble below the peak. The basic shape of the profile is the same as ESF 1 so

14

that the shortest bottomside background electron density gradient scale lengths $L \sim 10$ km and occur in the altitude range between 332 km and 378 km (note this is just 80 km higher than ESF 1). The largest linear growth rate (see Fig. 3), $\gamma_M = 6.07 \times 10^{-3}$ sec^{-1} and occurs at an altitude of 378 km where $\nu_R = 3.2 \times 10^{-5}$ sec^{-1}. This linear growth rate is a factor of six larger than the maximum growth rate in ESF 1. Unlike ESF 1 or 2, in ESF 3 the entire bottomside is linearly unstable. Between 332 km and 432 km the recombination term in Eq. (19) does not balance the gradient term. In this altitude range ν_R goes from 1.3×10^{-4} sec^{-1} to 6.4×10^{-6} sec^{-1} while γ goes from 2.5×10^{-3} sec^{-1} to 1×10^{-4} sec^{-1}. We also note again at the F peak, 434 km, $L = \infty$ and there is damping of the instability.

Figure 9 displays contour plots of constant n/n_o (or n_1/n_o) at $t = 300$, 700, 1000, and 1400 sec in the nonlinear evolution of ESF 3. Once again n_o as a function of altitude for this simulation is depicted in each of the frames. At $t = 300$ sec the early phase is exhibited with a 16% depletion contour with a maximum depletion inside this contour of 26%. The enhancement contour represents a 19% enhancement with a maximum 23% enhancement inside this contour. Clearly this simulation is developing more rapidly than either ESF 1 or 2. At $t = 700$ sec a rising bubble in the central x region is forming with an innermost depletion contour of 79%, with a maximum depletion inside this contour of 84%. Depletion contours of 16% in the wings are also in evidence. The innermost enhancement contour represents a 138% enhancement with a 187% enhancement maximum inside this contour. At $t = 1000$ sec we see the bubble rising past the F region peak. At this time the innermost depletion contour, in the high altitude portion of the bubble (near 430 km), represents an 85% depletion and there is a maximum depletion inside this contour of 85.2%. There is a long trail associated with the bubble at this time which extends about 100 km in altitude. However, the trail is not as well captured as in ESF 1. The depletions in the wings, near $|x| \sim 4$ km, exhibit an innermost contour of 58%

15

depletion. The enhanced regions at this time show an innermost contour of 572% enhancement with a maximum enhancement of 674% inside of this contour. Here we also note that the enhancements encompass a sizeable region in the x direction, but are confined to altitudes $\leqslant$ 390 km.

At t = 1400 sec (as far as ESF 3 was carried), the top of the main bubble in the central x region is at an altitude $\sim$ 500 km which is well beyond the F peak altitude of 434 km. Moreover, this bubble has a long trail connecting it to an altitude of 357 km. The widest part of the top outermost 16% depletion contour is $\sim$ 3 km; whereas, the innermost 58% depletion contour is $\sim$ 0.5 km wide. Therefore, this shows a long narrow bubble which extends $\sim$ 150 km in altitude and a few km in the east-west dimension. Radar backscatter observations (*Woodman and La Hoz*, 1976) have exhibited, on occasion, "plumes" to extend over 100 km in altitude. They have identified these plumes with regions of depleted plasma density. Within the innermost bubble contour at high altitudes, in Fig. 9 at 1400 sec, there is a maximum depletion of 70%. The innermost contour in the depleted wings represents a 96% depletion with a maximum depletion inside this contour of 97%. The innermost contour in the enhancement region corresponds to a 2590% enhancement with a maximum enhancement of 2640% inside this contour. Between t = 1000 sec and 1400 sec the top part of the bubble rose $\sim$ 65 km and this represents a rise velocity $\sim$ 160 m/sec. This is large compared with the 12 m/sec of ESF 1 and the 23 m/sec of ESF 2.

Figure 10 depicts contours of constant induced potential, ϕ_1, over the ESF 3 computational mesh at t = 1400 sec. Once again the more isolated high altitude part of the central bubble (see Fig. 9) is acted on by a dipolar like induced electric field pointing from west to east. This causes the bubble to rise with the $-(c/B)\nabla\phi_1 \times \hat{z}$ velocity. The outermost positive and negative potential contours are more closely spaced than in either ESF 1 or 2 and results

16

in a more rapid rise velocity. The lower portion of the mesh is acted on by an induced electric field which points from east to west and this is much weaker than the higher altitude electric field pointing from west to east. This causes the low altitude enhancements and depletions to remain at low altitudes and results in a capturing of the central portion of the rising bubble.

ESF O Case. Figure 11 depicts the n_o profile used in this simulation. The y extent is now between 242 km and 442 km with the F peak at 344 km. This is the same shape profile as ESF 1 except that the profile has been moved down 10 km. Consequently, the shortest bottomside background electron density gradient scale lengths $L \sim 10$ km and occur in the altitude range between 242 km and 288 km. The largest linear growth rate (see Fig. 3), $\gamma_M = 6.18 \times 10^{-4}$ sec^{-1} and occurs at an altitude of 288 km where $\nu_R = 5.12 \times 10^{-4}$ sec^{-1}. This linear growth rate is about 60% of the ESF 1 maximum linear growth rate. From Fig. 3 we note that the ESF O and ESF 1 growth rates are the same up to 288 km and both are stable below 274 km. In Fig. 3, ESF O shows instability between 274 km and 332 km. This is over a narrower altitude range than either ESF 1, 2, or 3 and represents weak instability. In this altitude range γ goes from 4.55×10^{-5} sec^{-1} to 3.94×10^{-5} sec^{-1} and ν_R goes from 7.98×10^{-4} sec^{-1} to 1.3×10^{-4} sec^{-1}.

Figure 11 depicts contour plots of constant n/n_o (or n_1/n_o) at $t = 5000$, 10,000 and 15,000 sec. At $t = 5000$ sec there is a 16% depletion contour with a maximum depletion inside this contour of 33%. There is a 19% enhancement contour with a maximum enhancement of 33% inside this contour. This shows a much slower development than ESF 1. At $t = 10,000$ sec a central bubble, disconnected from the lower depletion, appears to be rising toward the F peak. The depletion contour of this bubble is 16% with a maximum depletion of 24% inside this contour. There are 16% depletion contours in the wings at 290 km altitude near $|x| = 4$ km which have 37% maximum depletions inside of them. There is also a wide 19% enhancement contour with maximum enhancements inside the contour of 58%.

17

At $t = 15,000$ sec the bubble has risen very slowly and appears to be drying up. At this time the top of the rising bubble is at an altitude of 320 km and has the 16% depletion contour as at $t = 10,000$ sec, except over a smaller area. There is a maximum depletion of 29% inside the lower bubble (near 283 km) which also has a 16% depletion contour. In the wings, near 290 km altitude, there are 41% depletion contours with maximum depletions inside these contours of 44%. Inside the 19% enhancement contour is a maximum enhancement of 43%. In going from $t = 10,000$ sec to 15,000 sec both enhancements and depletions appear to be decaying, even though the main bubble is rising. At an altitude of 320 km $\nu_R^{-1} \sim 5000$ sec. Consequently, in this ESF O case, recombination plays a great role, especially considering the fact that the linear growth rates are not very large. Between 10,000 and 15,000 sec the top of the rising bubble has moved 12.5 km. This corresponds to a vertical rise velocity of 2.5 m/sec. Moreover, this 16% depletion contour in this rising bubble is ~ 0.7 km wide and is ~ 6 km long in the altitude direction. For ESF O, the enhancements and depletions are weak and, for the most part, reside in an altitude layer where 268 km $\leqslant y \leqslant$ 300 km (bottomside). In this layer, the bottomside gradient is sharp. This type of Spread F condition, i.e., ESF O, could correspond to the weak bottomside Spread F identified by *Woodman and La Hoz* [1976].

ESF O' and ESF O" Cases. Although we have not performed numerical simulations for these two cases, we can estimate the effects based on the four simulations presented. For ESF O', the n_o profile of ESF 1 was moved down 20 km, i.e., the F peak was at 334 km (10 km lower than ESF O). Here the shortest bottomside electron density gradient scale lengths, L $\sim$ 10 km and occur over an altitude range between 232 km and 278 km. For this case there is a very narrow region between 274 km and 280 km where linear instability occurs (see Fig. 4). The maximum growth rate, γ_M, is 2.15 $\times$ 10^{-4} sec^{-1} and occurs at an altitude of 278 km. This is almost an order of magnitude smaller growth rate than ESF 1 and one-third the growth rate of ESF O. From 232 km to 272 km the damping rate $-\gamma$ goes from 2.82 $\times$ 10^{-3} sec^{-1}

18

to $4.26 \times 10^{-5} \sec^{-1}$ (see Fig. 4). From 282 km to 432 km the damping rate goes from 2.27 $\times 10^{-4} \sec^{-1}$ to $1.27 \times 10^{-3} \sec^{-1}$ (also see Fig. 4). In ESF O there was a 60 km region of linear instability (growth) and here there is only a 6 km region of instability with smaller growth rates. Consequently, the time scale for development here would be even longer and the strength even smaller. Consequently, we would expect extremely weak spread F for ESF O'.

In the case of ESF O" the n_o profile of ESF 1 was moved down 50 km, i.e., the F peak was lowered to 304 km. Consequently, the shortest $L \sim 10$ km are in the range from 202 km to 248 km. However, in the entire range from 202 km to 402 km altitude, there is no linear instability. In this range the damping rate (see Fig. 4) goes from $8.75 \times 10^{-3} \sec^{-1}$ to 7.87 $\times 10^{-4} \sec^{-1}$ Consequently, no spread F would occur for this case ESF O".

IV. SUMMARY AND CONCLUSIONS

We have presented the results of four nonlinear numerical simulations of the collisional Rayleigh-Taylor instability for equatorial spread F geometry, using realistic altitude profiles for ion-neutral collision frequency, recombination rates and background electron density, in section III. Two other cases where the altitude of the F peak was lowered with respect to our canonical case ESF 1 were investigated via linear theory and conclusions were drawn based on the four numerical simulations. A summary of these results is presented in Table 2. We find that under favorable conditions, e.g., high altitude of the F peak (small effective ion-neutral collision frequency) and/or steep bottomside background electron density gradients, the collisional Rayleigh-Taylor instability causes linear growth on the bottomside of the F region. This in turn causes plasma density depletions or bubbles to be formed on the bottomside which then steepen on their top (see *Ossakow and Chaturvedi*, 1978) and nonlinearly rise to the topside by polarization (induced) $\mathbf{E} \times \mathbf{B}$ motion. This produces irregularities on the topside

19

where a linear analysis would predict no irregularities. High altitude of the F peak (h_p; see Table 2, ESF 3), small bottomside background electron density gradient scale lengths (L; see Table 2, ESF 2), and large percentage depletions (n_1/n_o) yield large vertical bubble rise velocities, V_B. Indeed, we have shown (see Table 2 and Section III) that changing the altitude of the F peak from 300 km to 430 km can have dramatic effects on the evolution of equatorial Spread F.

With relation to analytic studies of rising constant density, constant shape isolated equatorial Spread F bubbles in the collisional Rayleigh-Taylor regime, *Ossakow and Chaturvedi* [1978] have shown that the rise velocity is given by

$$V_B = \frac{g}{\nu_{in}} \frac{\frac{a}{b} \frac{n_1}{n_o}}{1 + \frac{a}{b}\left[1 - \frac{n_1}{n_o}\right]} \tag{29}$$

where a is one axis of the ellipse in the direction of $\mathbf{g}$, b is the other axis in the east-west direction, and n_1/n_o here is the fractional density depletion (a positive number in this formula). Applying Eq. (29) to the bubble velocities and n_1/n_o in Table 2, along with the appropriate value of ν_{in} (Fig. 2), we find that for ESF 0, 1, 2, and 3 $1 \lesssim a/b \lesssim 2$. This shows that in trying to model a steepening bubble, which has a density distribution inside of it, with a constant density-constant shaped bubble results in the preference of circular-like shapes. Furthermore, the greater bubble velocity of ESF 3 over ESF 1 can be understood as follows. Equation (29) and the general results of *Ossakow and Chaturvedi* [1978] show for the collisional Rayleigh-Taylor regime

$$V_B = \frac{g}{\nu_{in}} f(n_1/n_o) \tag{30}$$

20

where $f(n_1/n_o)$ is an increasing function of the fractional depletion n_1/n_o and depends on bubble shape. Raising the altitude of the F peak (as in ESF 3) decreases ν_{in}. Also in the ESF 3 simulation n_1/n_o is larger (see Table 2) and both factors tend to increase V_B. Furthermore, n_1/n_o is predicted to be larger in ESF 3 over ESF 1, at least according to linear theory, because $n_1 \propto \exp \gamma t$ where $\gamma \propto \nu_{in}^{-1}$ and is given by Eq. (19). Raising the height of the F peak increases the growth rate, γ. Thus, the ion-neutral collision frequency, ν_{in}, enters in two places in Eq. (30); whereas, the bottomside background scale length, L enters only in f (at least by the above argument). Similar arguments can be made in comparing ESF O and 2 with ESF 1.

To be sure we have not included a horizontal ambient zero order electric field, $\mathbf{E}_o$, in the problem. Inclusion of such a field would in the $\mathbf{E}_o \times \mathbf{B}$ drift frame not alter Eq. (11) and would modify Eq. (12) by adding a term of the form $\mathbf{E}_o \cdot \nabla (\nu_{in} \, n)$ to the right hand side (see also *Ossakow and Chaturvedi*, 1978). This would also alter Eq. (19), for example by changing it to

$$\gamma = \frac{1}{L} \left(\frac{g}{\nu_{in}} + \frac{cE_o}{B} \right) - \nu_R$$

(31)

where E_o is positive if in the eastward direction and negative if in the westward direction. Large enough values of a westward E_o could, depending on altitude of the F peak, result in stability. Any eastward E_o will make the instability grow faster. Similarly an eastward E_o will make the bubbles rise faster and a westward E_o will slow them down (see *Ossakow and Chaturvedi*, 1978). In any case, future studies including this effect and the effect of a horizontal neutral wind, $\mathbf{V}_n$, (see *Ossakow and Chaturvedi*, 1978) are being planned.

21

Our present studies have been restrictive in the east-west (x) dimension to bubble spatial sizes ~ 1 km in this direction (total x dimension $= 8$ km). Our preliminary results from long wavelength (~ 50-100 km) perturbation numerical simulations (*Zalesak et al.*, 1978) show that large transverse (east-west) bubble sizes may be generated by the nonlinear evolution of the collisional Rayleigh-Taylor instability: *McClure et al.* [1977] have also observed large transverse bubble dimensions. Future numerical simulation plans also include using random initial perturbations.

Our present numerical simulation studies as explicitly stated only covers the collisional Rayleigh-Taylor regime. This allows for the algebraic solution of the ion and electron momentum equations (see Eqs. (6) and (7)) and results in having to solve only two equations (Eqs. (11) and (12)) numerically. Including inertial effects and thus being able to handle the collisionless Rayleigh-Taylor regime requires solving the *full* two dimensional vector ion momentum equation (2) with the electrons still being described by Eq. (6). This is in addition to solving a continuity equation (1) and the divergence of the current equal to zero equation (8). Future plans call for making these changes. However, it should be pointed out that the range of validity of the collisional Rayleigh-Taylor regime requires $\nu_{in}^2 > 4g/L$ (see for example *Hudson and Kennel*, 1975; *Ossakow and Chaturvedi*, 1978). Consequently, if we take L to be the bubble scale length, larger bubbles will remain in the collisional Rayleigh-Taylor regime to higher altitudes.

The physical picture of equatorial Spread F that emerges from our present simulation studies can be described as follows. After sunset the E region begins to recombine. Due to recombination and electrodynamic effects (or just recombination) the bottomside F region background electron density gradient begins to steepen. The electrodynamic effects are such that an eastward ambient electric field causes the bottomside density gradient to steepen and the F region to rise much akin to how a barium cloud would steepen and rise in equatorial

22

geometry (see *Ossakow and Chaturvedi*, 1978). Thus, the equatorial F region ionosphere can be viewed as a giant barium cloud (with inhomogeneities in the east-west direction occuring over very large spatial scale lengths). Indeed, our present studies of the nonlinear evolution of the collisional Rayleigh-Taylor instability are similar to our barium cloud striation studies (see *Scannapieco and Ossakow*, 1976; *Scannapieco et al.*, 1976), except that the geometry has been rotated and gravity substitutes for an ambient electric field as the driving force. This steepening and rise can also be caused by a downward motion of the neutral atmosphere. When the altitude is high enough and/or bottomside background electron density gradients steep enough to overcome recombination effects density fluctuations will begin to grow (become linearly unstable) on the bottomside. If these altitude and gradient conditions are right plasma density depletions (bubbles) will form on the bottomside. Similarly, if these conditions are right these bubbles will then nonlinearly rise by polarization $\mathbf{E} \times \mathbf{B}$ motion through the F peak and cause topside Spread F. Although the present series of simulations did not resolve meter size irregularities (in the present simulations $\Delta y = 2$ km and $\Delta x = 200$ meters), it is expected that the steepening bubbles, rising through the peak, will bifurcate (see for example *Ossakow et al*, 1977) on its topside and produce shorter and shorter wavelength irregularities either by a cascade or two step mechanism. For example, the gradients associated with the longer wavelength (~ 100 m-1 km) unstable fluid-type collisional Rayleigh-Taylor modes could result in shorter wavelength (~ 1 m) explosive growth kinetic instabilities.

Finally, we wish to compare our numerical simulation results with some of the experimental observations. The phenomenon of rising equatorial Spread F bubbles has been observed by rocket (*Kelley et al.*, 1976) and satellite (*McClure et al.*, 1977) in situ measurements and inferred from radar backscatter "plume" measurements (*Woodman and LaHoz*, 1976). The range of upward bubble velocities, depending on ambient ionospheric conditions, e.g. height of F peak and bottomside gradient scale length, in our simulations can account for many of the

23

experimental observations regarding the range of upward velocities reported by *McClure et al.* [1977]. To be sure a satellite is making a single point measurement and does not have all the background ionospheric driving conditions (coordinated measurements with ground based experiments and possibly rocket in situ measurements are needed). Nevertheless, the agreement between the simulations and the data (*McClure et al.*, 1977) is quite good. The dependence of the phenomena on high ionospheres, from the three meter backscatter results, has been noted by *Farley et al.* [1970] and *Woodman and La Hoz* [1976]. It should be pointed out that the 50 MHz (3 meter irregularities) backscatter is just a signature. Its full physical relation to the longer wavelength Rayleigh-Taylor modes, which can cause Spread F observed on iononograms and satellite transmission scintillation effects, is not unequivocally understood at this point. The long (in altitude) radar plume measurements (*Woodman and LaHoz*, 1976) could be related to the long bubbles (e.g., see ESF 3 and Fig. 9) connecting high and low altitudes (also see previous discussion in this section). The thin layer of bottomside irregularities observed by *Woodman and La Hoz* [1976] could be accounted for by having a low ionosphere, e.g., our numerical simulation results from ESF O and O'. Recently (August 1977), a coordinated equatorial F region measurement campaign was performed under the auspices of the Defense Nuclear Agency (DNA) at Kwajalein in the Marshall Islands. Some of the preliminary results from ionosonde (Drs. Bibl and Reinisch, University of Lowell), 1 meter (150 MHz) ALTAIR radar backscatter (Dr. Towle, MIT Lincoln Labs), and DNA Wideband, ATS-6 and Navy Transit satellite scintillation measurements (Drs. Baron, Tsunoda, Cousins and Livingston, SRI) agree with the results of the present numerical simulations, which depend on altitude of the F peak and steepness of the bottomside background electron density gradient.

Acknowledgement

References

Balsley, B.B., G. Haerendel and R.A. Greenwald, Equatorial Spread F: Recent observations and a new interpretation, *J. Geophys. Res., 77*, 5625, 1972.

Boris, J.P., and D.L. Book, Flux-corrected transport. I. SHASTA, a fluid transport algorithm that works, *J. Comp. Phys. 11*, 38, 1973.

Chaturvedi, P.K., and P.K. Kaw, Steady state finite amplitude Rayleigh Taylor modes in Spread F, *Geophys. Res. Letts., 2*, 381, 1975a.

Chaturvedi, P.K., and P.K. Kaw, Correction, *Geophys. Res. Letts., 2*, 499, 1975b.

Chaturvedi, P., and P. Kaw, An interpretation for the power spectrum of Spread F irregularities, *J. Geophys. Res. 81*, 3257, 1976.

Chaturvedi, P.K., and S.L. Ossakow, Nonlinear Theory of the collisional Rayleigh-Taylor instability in equatorial Spread F, *Geophys. Res. Letts., 4*, 558, 1977.

Costa, E., and M.C. Kelley, On the role of steepened structures and drift waves in equatorial Spread F, *J. Geophys. Res.* (submitted 1978a).

Costa, E., and M.C. Kelley, Linear theory for the collisionless drift wave instability with wavelengths near the ion gyroradius, *J. Geophys. Res.* (submitted 1978b).

Dyson, P.L., J. P. McClure and W.B. Hanson, In situ measurements of the spectral characteristics of F region ionospheric irregularities, *J. Geophys. Res. 79*, 1497, 1974.

Farley, D.T., B.B. Balsley, R.F. Woodman, and J.P. McClure, Equatorial Spread F: Implications of VHF radar observations, *J. Geophys. Res., 75*, 7199, 1970.

Haerendel, G., Theory of Equatorial Spread F, preprint, Max-Planck Institute fur Physik und Astrophysik, 1974.

Hudson, M.K., Spread F Bubbles: Nonlinear Rayleigh-Taylor mode in two dimensions, *J. Geophys. Res.* (to be published 1978).

Hudson, M.K., and C.F. Kennel, Linear theory of equatorial Spread F, *J. Geophys. Res., 80*, 4581, 1975.

Kelley, M.C., G. Haerendel, H. Kappler, A. Valenzuela, B.B. Balsley, D.A. Carter, W.L. Ecklund, C.W. Carlson, B. Hausler, and R. Torbert, Evidence for a Rayleigh-Taylor type instability and upwelling of depleted density regions during equatorial spread F, *Geophys. Res. Letts.*, *3*, 448, 1976.

Kelley, M.C., and E. Ott, Two-dimensional turbulence in equatorial Spread F, *J. Geophys. Res.* (submitted 1978).

McClure, J.P., W.B. Hanson, and J.H. Hoffman, Plasma bubbles and irregularities in the equatorial ionosphere, *J. Geophys. Res. 82*, 2650, 1977.

McDonald, B.E., Explicit Chebychev-iterative solution of nonself-adjoint elliptic equations on a vector computer, NRL Memorandum Report 3541, June 1977.

McFarland, M., D.L. Albritton, F.C. Fehsenfeld, E.E. Ferguson, and A.L. Schmeltekopf, Flow-drift technique for ion mobility and *ion-molecule reaction* rate constant measurements. II. Positive ion reactions of N^+, O^+ and N_2^+ with O_2 and O^+ with N_2 from thermal to ~2 eV, *J. Chem. Phys., 59*, 6620, 1973.

Morse, F.A., B.C. Edgar, H.C. Koons, C.J. Rice, W.J. Heikkila, J.H. Hoffman, B.A. Tinsley, J.D. Winningham, A.B. Christensen, R.F. Woodman, J. Pomalaza, and N.R. Teixeira, Equion, an equatorial ionospheric irregularity experiment, *J. Geophys. Res., 82*, 578, 1977.

Ossakow, S.L., and P.K. Chaturvedi, Morphological studies of rising equatorial Spread F bubbles, *J. Geophys. Res.* (in press 1978).

Ossakow, S.L., S.T. Zalesak, and N.J. Zabusky, Recent results on cleavage, bifurcation, and cascade mechanisms in ionospheric plasma clouds, NRL Memo Report 3579, August 1977.

Ossakow, S.L., S.T. Zalesak, B.E. McDonald, and P.K. Chaturvedi, Theoretical and numerical simulation predictions of the equatorial Spread F environment, in *Proceedings of 1978 Symposium on the Effect of the Ionosphere on Space and Terrestrial Systems*, edited by J.M. Goodman, U.S. Government Printing Office, Washington, D.C., 1978.

Ott, E., Theory of Rayleigh-Taylor bubbles in the equatorial ionosphere, *J. Geophys. Res.* (in

press 1978).

Scannapieco, A.J., and S.L. Ossakow, Nonlinear equatorial Spread F, *Geophys. Res. Letts., 3,* 451, 1976.

Scannapieco, A.J., S.L. Ossakow, S.R. Goldman, and J.M. Pierre, Plasma cloud late time striation spectra, *J. Geophys. Res., 81,* 6037, 1976.

Strobel, D.F., and M.B. McElroy, The F2-layer at middle latitudes, *Planet. Space Sci., 18,* 1181, 1970.

Szuszczewicz, E.P., Ionospheric holes and equatorial spread F: chemistry and transport, *J. Geophys. Res.* (in press 1978).

Woodman, R.F. and C. La Hoz, Radar observations of F region equatorial irregularities, *J. Geophys. Res. 81,* 5447, 1976.

Zalesak, S.T., S.L. Ossakow, B.E. McDonald, and P.K. Chaturvedi, Numerical simulations of nonlinear equatorial Spread F, EOS, *Trans. Am. Geophys. Un., 58,* 1202, 1977. Abstract.

Zalesak, S.T., S.L. Ossakow, B.E. McDonald, and P.K. Chaturvedi, Spatially large equatorial Spread F bubbles, *Trans. Am. Geophys. Un., 59,* (1978 Spring Meeting, in press).

Table 1 — Numerical simulation cases considered.

ESF	Height of F peak, h_p (km)	Minimum bottomside Scale length, L (km)
0	344	10
1	354	10
2	354	5
3	434	10

Table 2 — Results of Numerical Studies. Note the bubble rise velocity V_B, and the fractional depletion n_1/n_o refer to the values near the F peak altitude.

| ESF	Altitude of F peak, h_p(km)	Minimum bottomside Scale length, L(km)	Bubble rise Velocity, V_B(m/sec)	Percentage depletion n_1/n_o	Resulting Conditions
1	354	10	~12	~40%	Maximum linear growth rate $\gamma_M \sim 10^{-3}$ sec^{-1}. Bottomside linear instability from 274 to 350 km altitude. Bubble passes peak ~ 8000 sec. Moderate top and bottomside Spread F with simulation stopped at 10^4 sec.
2	354	5	~23	~60%	$\gamma_M \sim 3.2 \times 10^{-3}$ sec^{-1}. Bottomside linear instability from 282 to 352 km altitude. Bubble passes peak ~ 4000 sec. Strong bottomside and moderate topside Spread F with simulation stopped at 5000 sec.
3	434	10	~160	~85%	$\gamma_M \sim 6 \times 10^{-3}$ sec^{-1}. Entire bottomside from 332 to 434 km linearly unstable. Bubble passes peak ~ 10^3 sec. Strong bottomside and topside Spread F with simulation stopped at 1400 sec.
0	344	10	~2.5	~16%	$\gamma_M \sim 6 \times 10^{-4}$ sec^{-1}. Bottomside linearly unstable from 274 to 332 km. Bubble does not get to F peak rather dries up due to recombination. Weak bottomside Spread F only with simulation stopped at 15,000 sec.
O'	334	10	Undetermined	Undetermined	$\gamma_M \sim 2 \times 10^{-4}$ sec^{-1}. Narrow bottomside region between 274 and 280 km linearly unstable. This would result in extremely weak bottomside Spread F. No nonlinear simulation performed.
O"	304	10	None	None	Entire bottomside between 202 and 304 km is linearly stable. No Spread F and no nonlinear simulation performed.

29

EQUATORIAL SPREAD F GEOMETRY
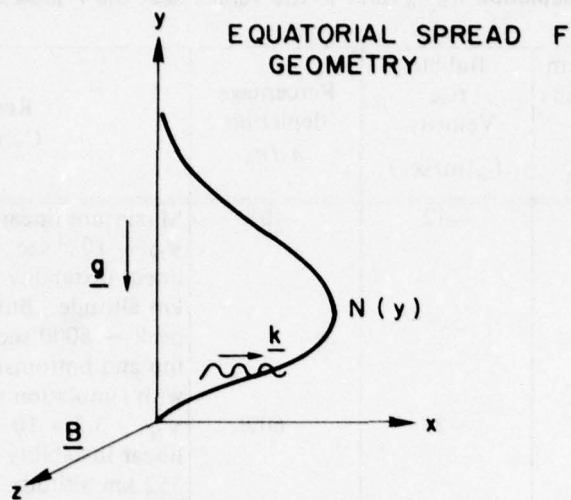
Fig. 1 - Equatorial Spread F geometry. $N(y)$ represents the ambient electron density profile and has only altitude (y) dependence. **B** points to the north, x is west and so **g** x **B** is to the east. A horizontal perturbation is denoted by **k**.
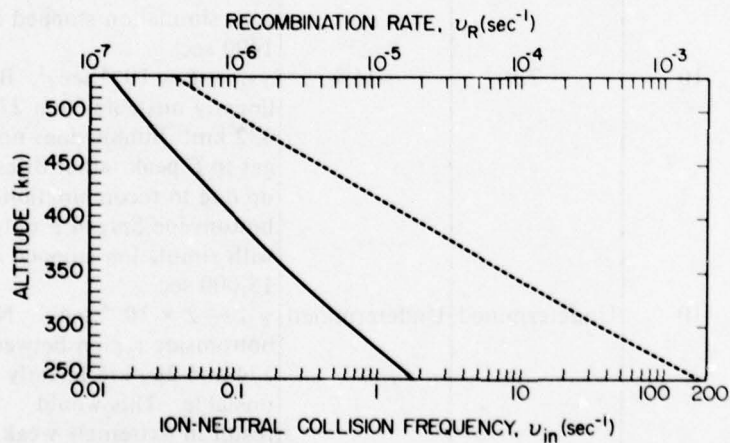
Fig. 2 - Ion-neutral collision frequency (solid line), ν_{in}, and recombination rate (dashed line), ν_R, as a function of altitude. The altitude range encompasses those altitudes used in the numerical simulations.
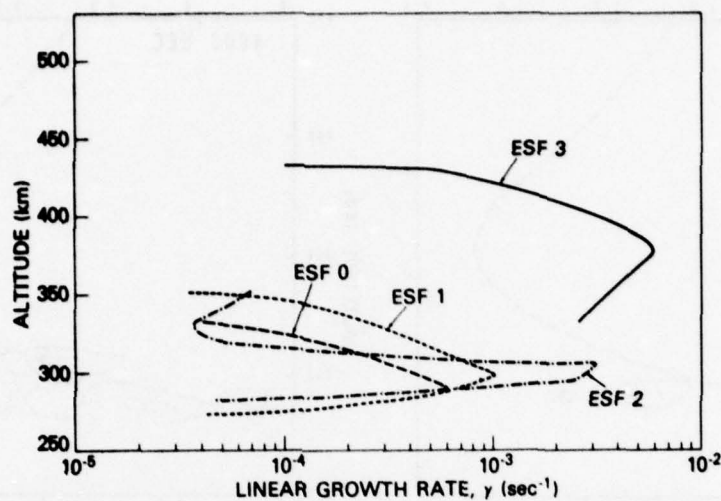
30

Fig. 3 – Linear growth rate, γ, versus altitude for the four numerical simulations ESF O, ESF 1, 2, and 3 (see Table 1). A horizontal perturbation was assumed. Only the regions of instability are plotted for these four cases.
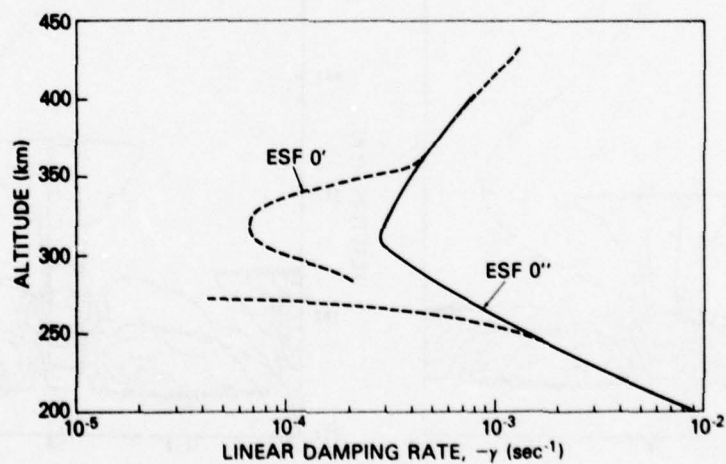

Fig. 4 – Linear damping rate, $-\gamma$, versus altitude for ESF O'and O". ESF O is the same shape as ESF 1 with the F peak moved down 20 km; similarly ESF O" has the F peak moved down 50 km. A horizontal perturbation was assumed. Only the regions of stability have been plotted for these two cases.

31
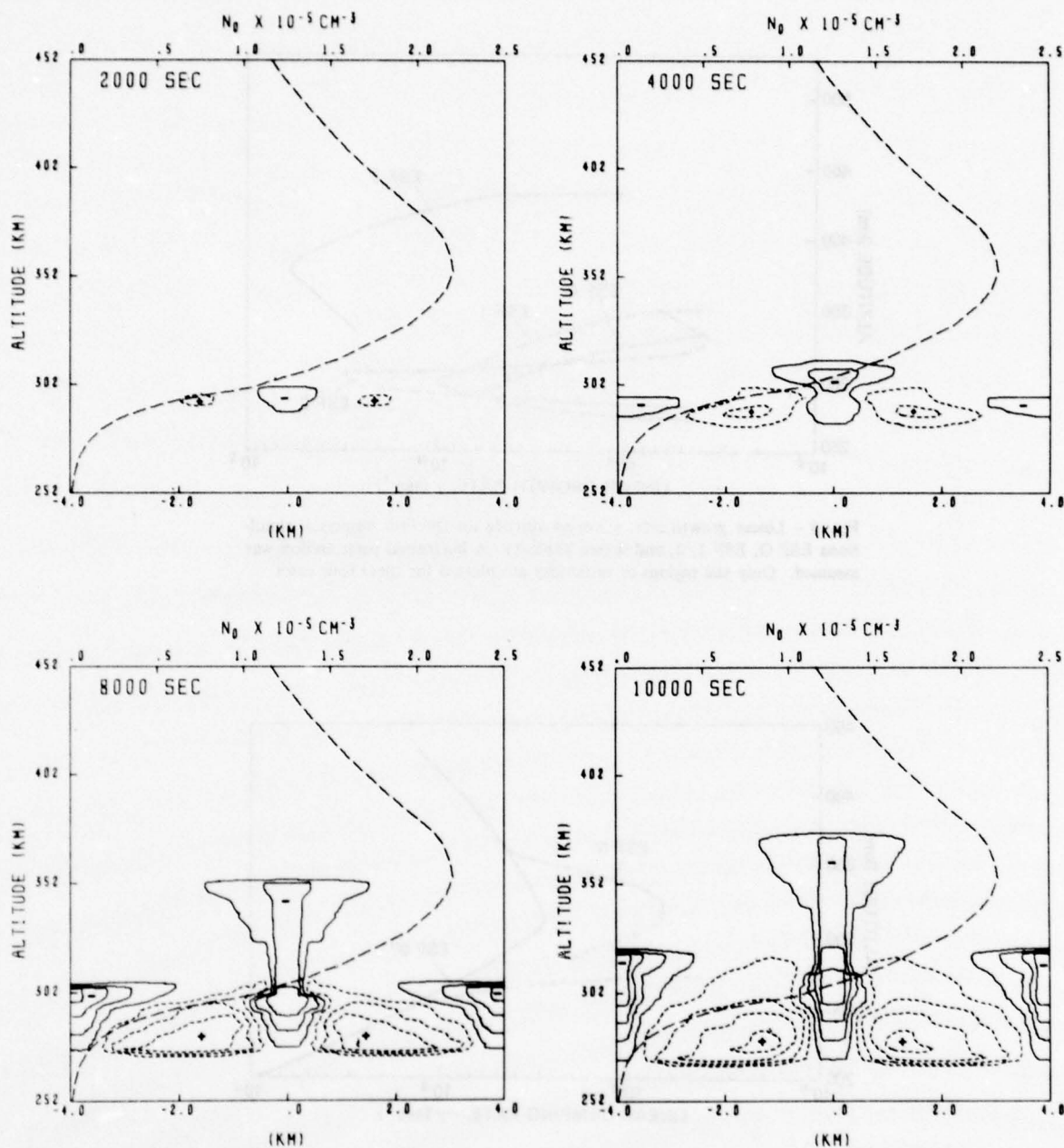
Fig. 5 – Contour plots of constant n_1/n_0 for the simulation ESF 1 at t = 2000, 4000, 8000, and 10,000 sec. The small dashed contours with a plus sign inside and the solid contours with a minus sign inside indicate enhancement and depletions over the ambient electron number density. The large dashed curve depicts the ambient electron number density (values on upper horizontal axis), n_0, as a function of altitude. The vertical y axis represents altitude, the lower horizontal x axis is east-west range, and the ambient magnetic field is along the z axis, out of the figure.
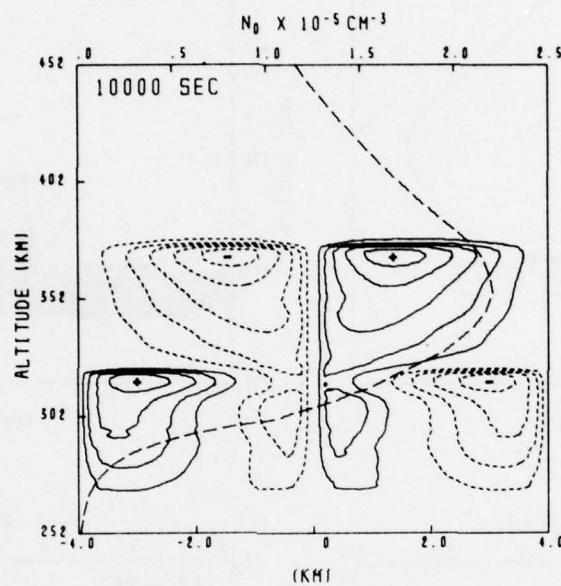
Fig. 6 – Contours of constant induced (polarization) potential, ϕ_1, over the ESF 1 mesh (see Fig. 5) at $t = 10,000$ sec. Plus and minus denote positive and negative values, with values decreasing in magnitude as one goes from the innermost to the outermost contours. The large dashed curve is n_o.

Fig. 7 – Contour plots of constant n_1/n_0 for the ESF 2 simulation at t = 1000, 3000, 4000, and 5000 sec. All other nomenclature is the same as Fig. 5.

34

Fig. 8 – Contours of constant induced potential, ϕ_1, over the
ESF 2 mesh (see Fig. 7) at $t = 5000$ sec. All other nomen-
clature is same as Fig. 6.

Fig. 9 – Contour plots of constant n_1/n_0 for the ESF 3 simulation at t = 300, 700, 1000, and 1400 sec. All other nomenclature is same as Fig. 5.

36
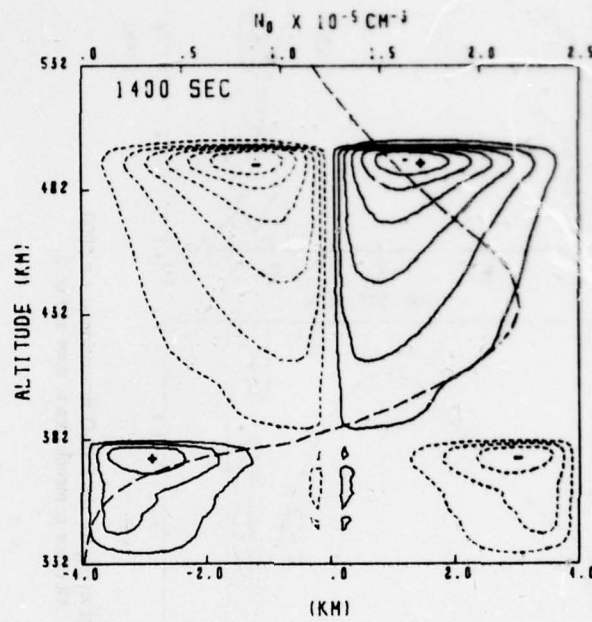
Fig. 10 – Contours of constant induced potential, ϕ_1, over the ESF 3 mesh (see Fig. 9) at $t = 1400$ sec. All other nomenclature is same as Fig. 6.
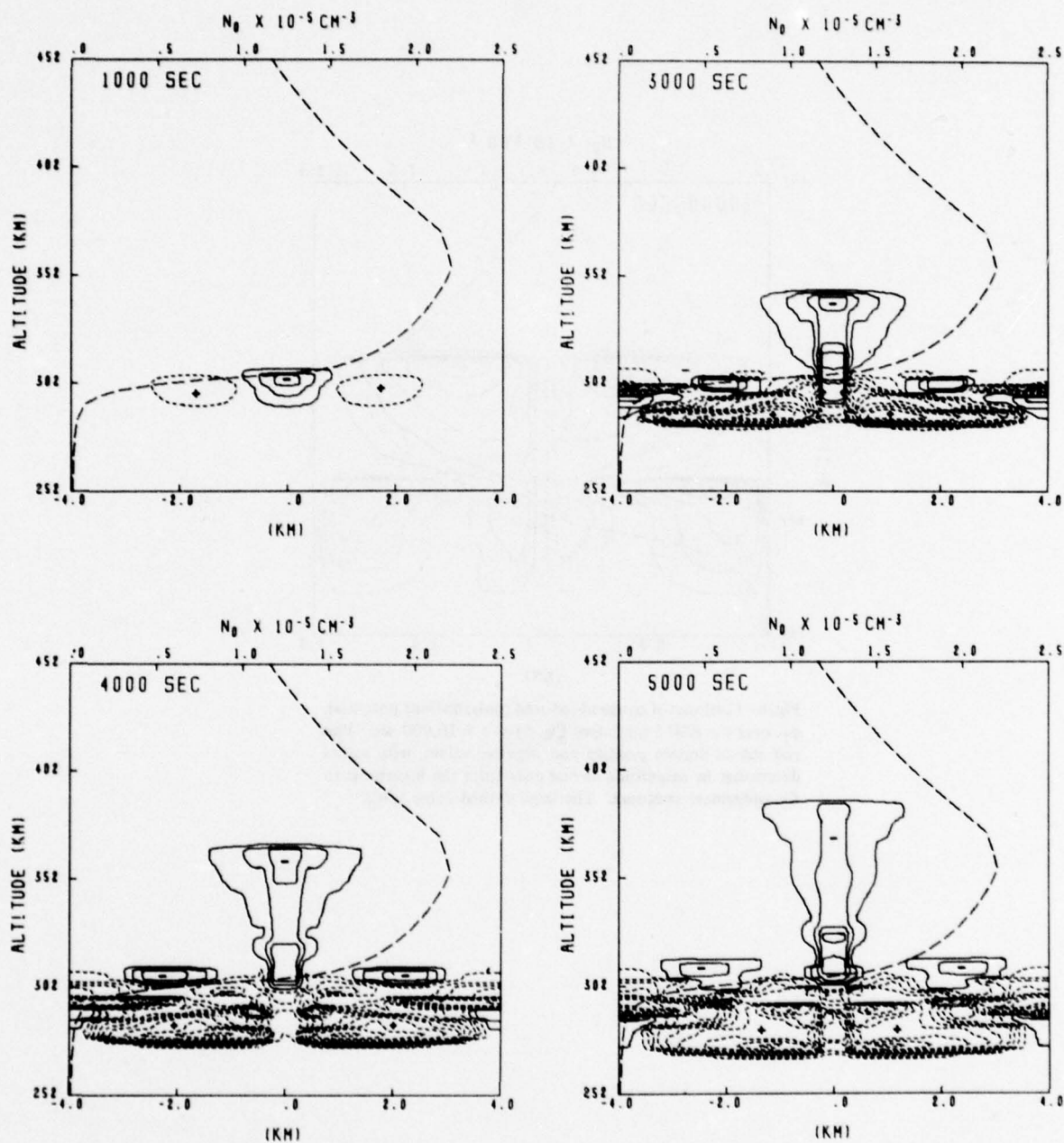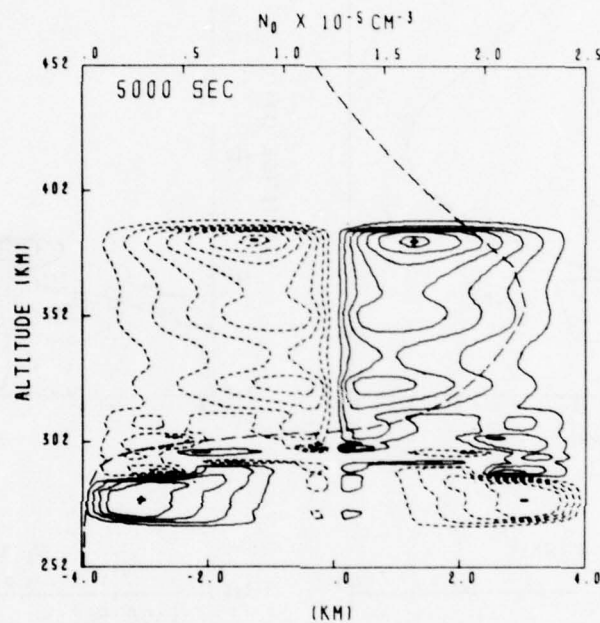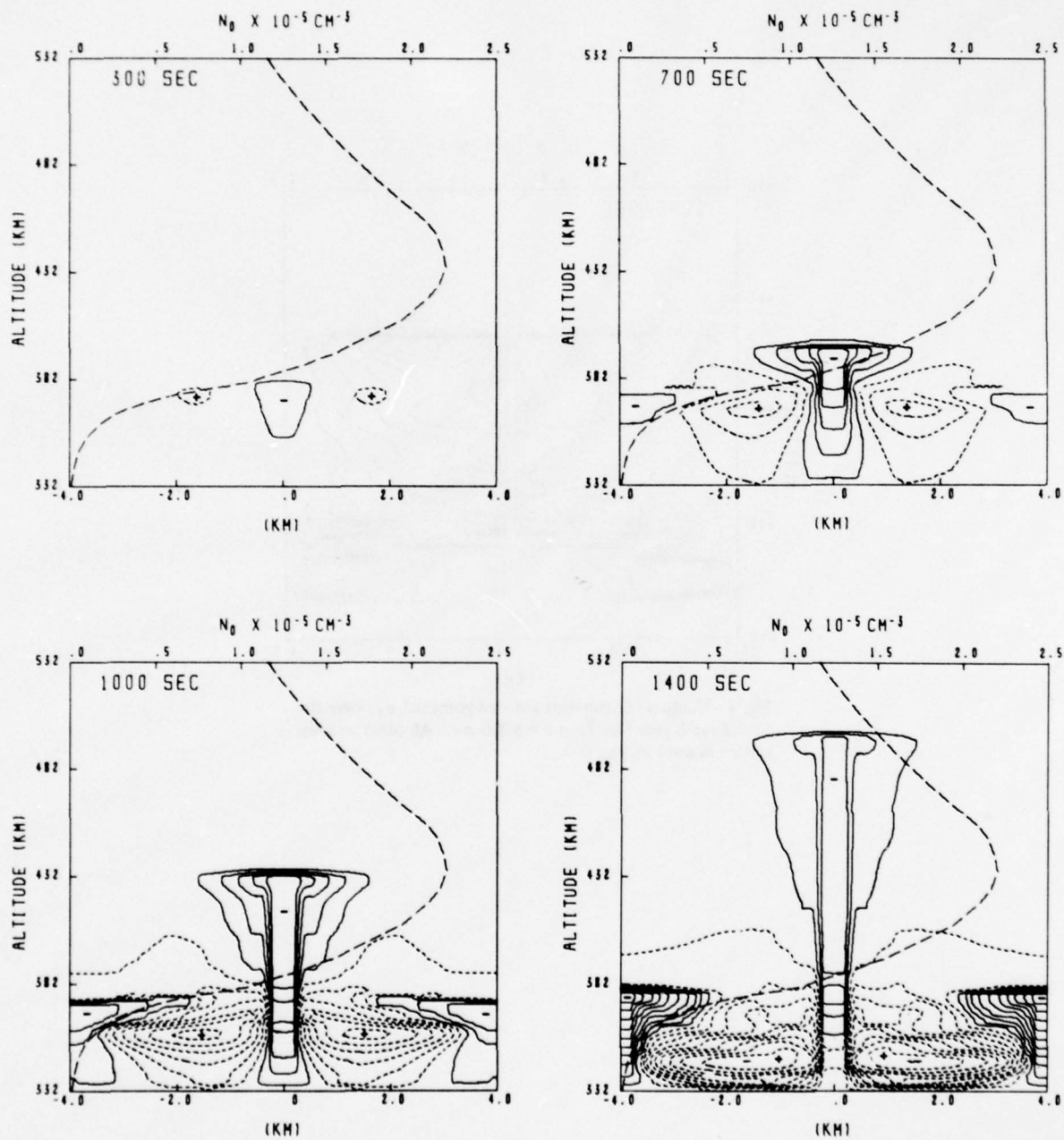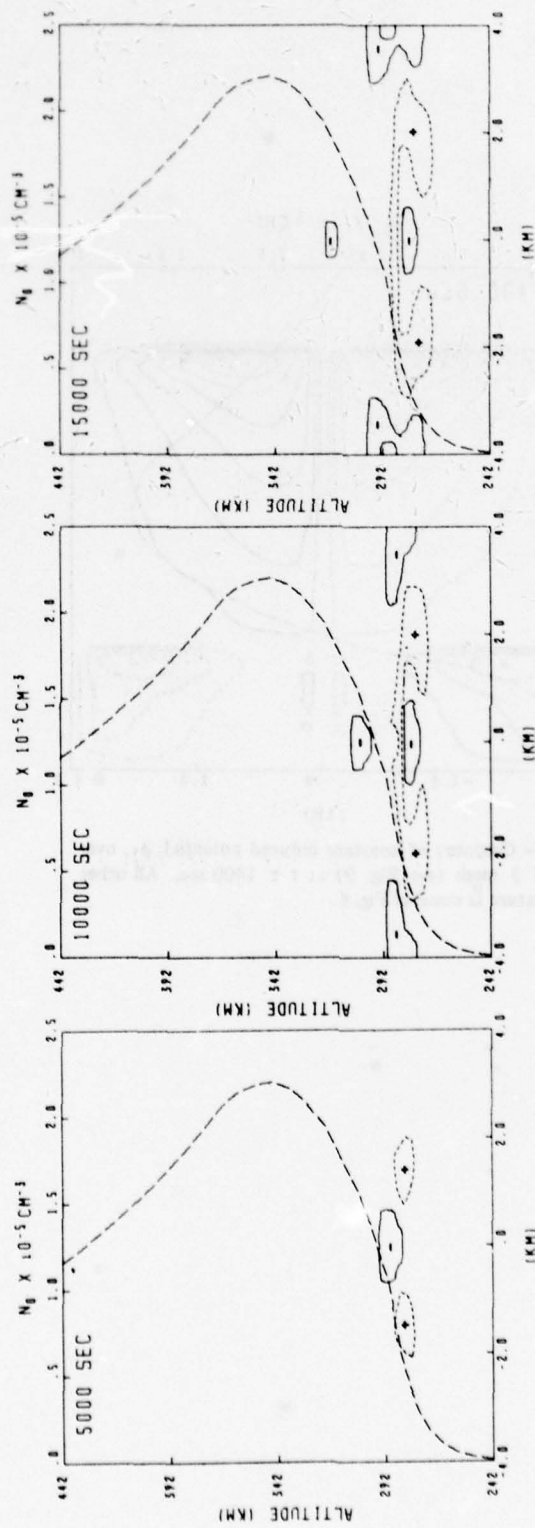
Fig. 11 — Contours of constant n_1/n_0 for the ESF O simulation at $t = 5000$, 10,000, and 15,000 sec. All other nomenclature is same as Fig. 5.

38

DISTRIBUTION LIST

DEPARTMENT OF DEFENSE

ASSISTANT SECRETARY OF DEFENSE
COMM, CMD, CONT & INTELL
WASHINGTON, D.C. 20301
    01CY ATTN J. BABCOCK
    01CY ATTN M. EPSTEIN

ASSISTANT TO THE SECRETARY OF DEFENSE
ATOMIC ENERGY
WASHINGTON, D.C. 20301
    01CY ATTN EXECUTIVE ASSISTANT

DIRECTOR
COMMAND CONTROL TECHNICAL CENTER
PENTAGON RM BE 685
WASHINGTON, D.C. 20301
    01CY ATTN C-650
    01CY ATTN C-312 R. MASON

DIRECTOR
DEFENSE ADVANCED RSCH PROJ AGENCY
ARCHITECT BUILDING
1400 WILSON BLVD.
ARLINGTON, VA. 22209
    01CY ATTN NUCLEAR MONITORING RESEARCH
    01CY ATTN STRATEGIC TECH OFFICE

DEFENSE COMMUNICATION ENGINEER CENTER
1860 WIEHLE AVENUE
RESTON, VA. 22090
    01CY ATTN CODE R820
    01CY ATTN CODE R410   JAMES W. MCLEAN
    01CY ATTN CODE R720   J. WORTHINGTON

DIRECTOR
DEFENSE COMMUNICATIONS AGENCY
WASHINGTON, D.C. 20305
        (ADR CNWDI: ATTN CODE 240 FOR)
    01CY ATTN CODE 480
    01CY ATTN CODE 810 R. W. ROSTRON
    01CY ATTN CODE 101B
    01CY ATTN CODE 103 M. RAFFENSPERGER

DEFENSE DOCUMENTATION CENTER
CAMERON STATION
ALEXANDRIA, VA. 22314
    (12 COPIES IF OPEN PUBLICATION, OTHERWISE 2 COPIES)
    12CY ATTN TC

DIRECTOR
DEFENSE INTELLIGENCE AGENCY
WASHINGTON, D.C. 20301
    01CY ATTN DT-1B
    01CY ATTN DB-4C E. O'FARRELL
    01CY ATTN DIAAP A. WISE
    01CY ATTN DIAST-5
    01CY ATTN DT-1BZ R. MORTON
    01CY ATTN HQ-TR J. STEWART
    01CY ATTN W. WITTIG DC-7D

DIRECTOR
DEFENSE NUCLEAR AGENCY
WASHINGTON, D.C. 20305
    01CY ATTN STVL
    04CY ATTN TITL
    01CY ATTN DDST
    03CY ATTN RAAE

COMMANDER
FIELD COMMAND
DEFENSE NUCLEAR AGENCY
KIRTLAND AFB, NM 87115
    01CY ATTN FCPR

DIRECTOR
INTERSERVICE NUCLEAR WEAPONS SCHOOL
KIRTLAND AFB, NM 87115
    01CY ATTN DOCUMENT CONTROL

JOINT CHIEFS OF STAFF
WASHINGTON, D.C. 20301
    01CY ATTN J-3 WWMCCS EVALUATION OFFICE

DIRECTOR
JOINT STRAT TGT PLANNING STAFF
OFFUTT AFB
OMAHA, NB 68113
    01CY ATTN JLTW-2
    01CY ATTN JPST G. GOETZ

CHIEF
LIVERMORE DIVISION FLD COMMAND DNA
DEPARTMENT OF DEFENSE
LAWRENCE LIVERMORE LABORATORY
P. O. BOX 808
LIVERMORE, CA 94550
    01CY ATTN FCPRL

2

DIRECTOR
NATIONAL SECURITY AGENCY
DEPARTMENT OF DEFENSE
FT. GEORGE G. MEADE, MD 20755
    01CY ATTN JOHN SKILLMAN R52
    01CY ATTN FRANK LEONARD
    01CY ATTN W14 PAT CLARK
    01CY ATTN OLIVER H. BARTLETT W32
    01CY ATTN R5

COMMANDANT
NATO SCHOOL (SHAPE)
APO NEW YORK 09172
    01CY ATTN U.S. DOCUMENTS OFFICER

UNDER SECY OF DEF FOR RSCH & ENGRG
DEPARTMENT OF DEFENSE
WASHINGTON, D.C. 20301
    01CY ATTN STRATEGIC & SPACE SYSTEMS (OS)

WWMCCS SYSTEM ENGINEERING ORG
WASHINGTON, D.C. 20305
    01CY ATTN R. CRAWFORD

COMMANDER/DIRECTOR
ATMOSPHERIC SCIENCES LABORATORY
U.S. ARMY ELECTRONICS COMMAND
WHITE SANDS MISSILE RANGE, NM 88002
    01CY ATTN DELAS-EO F. NILES

DIRECTOR
BMD ADVANCED TECH CTR
HUNTSVILLE OFFICE
P. O. BOX 1500
HUNTSVILLE, AL 35807
    01CY ATTN ATC-T MELVIN T. CAPPS
    01CY ATTN ATC-O W. DAVIES
    01CY ATTN ATC-R DON RUSS

PROGRAM MANAGER
BMD PROGRAM OFFICE
5001 EISENHOWER AVENUE
ALEXANDRIA, VA 22333
    01CY ATTN DACS-BMT J. SHEA

CHIEF C-E SERVICES DIVISION
U.S. ARMY COMMUNICATIONS CMD
PENTAGON RM 1B269
WASHINGTON, D.C. 20310
    01CY ATTN C-E-SERVICES DIVISION

3

COMMANDER
FRADCOM TECHNICAL SUPPORT ACTIVITY
DEPARTMENT OF THE ARMY
FORT MONMOUTH, N.J. 07703
    01CY   ATTN DRSEL-NL-RD H. BENNET
    01CY   ATTN DRSEL-PL-ENV H. BOMKE
    01CY   ATTN J. E. QUIGLEY

COMMANDER
HARRY DIAMOND LABORATORIES
DEPARTMENT OF THE ARMY
2800 POWDER MILL ROAD
ADELPHI, MD 20783
       (CNWDI-INNER ENVELOPE: ATTN: DELHD-RBH)
    01CY   ATTN DELHD-TI M. WEINER
    01CY   ATTN DELHD-RB R. WILLIAMS
    01CY   ATTN DELHD-NP F. WIMENITZ
    01CY   ATTN DELHD-NP C. MOAZED

COMMANDER
U.S. ARMY COMM-ELEC ENGRG INSTAL AGY
FT. HUACHUCA, AZ 85613

    01CY   ATTN CCC-EMEO GEORGE LANE

COMMANDER
U.S. ARMY FOREIGN SCIENCE & TECH CTR
220 7TH STREET, NE
CHARLOTTESVILLE, VA 22901
    01CY   ATTN DRXST-SD
    01CY   ATTN R. JONES

COMMANDER
U.S. ARMY MATERIEL DEV & READINESS CMD
5001 EISENHOWER AVENUE
ALEXANDRIA, VA 22333
    01CY   ATTN DRCLDC J. A. BENDER

4

COMMANDER
U.S. ARMY NUCLEAR AND CHEMICAL AGENCY
7500 BACKLICK ROAD
BLDG 2073
SPRINGFIELD, VA 22150
    01CY   ATTN LIBRARY

DIRECTOR
U.S. ARMY BALLISTIC RESEARCH LABS
ABERDEEN PROVING GROUND, MD 21005
    01CY   ATTN TECH LIB   EDWARD BAICY

COMMANDER
U.S. ARMY SATCOM AGENCY
FT. MONMOUTH, NJ 07703
    01CY   ATTN DOCUMENT CONTROL

COMMANDER
U.S. ARMY MISSILE INTELLIGENCE AGENCY
REDSTONE ARSENAL, AL 35809
    01CY   ATTN JIM GAMBLE

DIRECTOR
U.S. ARMY TRADOC SYSTEMS ANALYSIS ACTIVITY
WHITE SANDS MISSILE RANGE, NM 88002
    01CY   ATTN ATAA-SA
    01CY   ATTN TCC/F. PAYAN JR.
    01CY   ATTN ATAA-TAC LTC J. HESSE

COMMANDER
NAVAL ELECTRONIC SYSTEMS COMMAND
WASHINGTON, D.C. 20360
    01CY   ATTN NAVALEX 034 T. HUGHES
    01CY   ATTN PME 117
    01CY   ATTN PME 117-T
    01CY   ATTN CODE 5011

COMMANDING OFFICER
NAVAL INTELLIGENCE SUPPORT CTR
4301 SUITLAND ROAD, BLDG. 5
WASHINGTON, D.C. 20390
    01CY   ATTN MR. DUBBIN STIC 12
    01CY   ATTN NISC-50
    01CY   ATTN CODE 5404 J. GALET

COMMANDER
NAVAL OCEAN SYSTEMS CENTER
SAN DIEGO, CA 92152
    03CY ATTN CODE 532 W. MOLER
    01CY ATTN CODE 0230 C. BAGGETT
    01CY ATTN CODE 81 R. EASTMAN

DIRECTOR
NAVAL RESEARCH LABORATORY
WASHINGTON, D.C. 20375
    01CY ATTN CODE 6700 TIMOTHY P. COFFEY (25 CYS IF UNCLASS, 1 CY IF CLASS)
    01CY ATTN CODE 6701 JACK D. BROWN
    01CY ATTN CODE 6780 BRANCH HEAD (150 CYS IF UNCLASS, 1 CY IF CLASS)
    01CY ATTN CODE 7500 HQ COMM DIR BRUCE WALD
    01CY ATTN CODE 7550 J. DAVIS
    01CY ATTN CODE 7580
    01CY ATTN CODE 7551
    01CY ATTN CODE 7555
    01CY ATTN CODE 6730 E. MCLEAN
    01CY ATTN CODE 7127 C. JOHNSON

COMMANDER
NAVAL SEA SYSTEMS COMMAND
WASHINGTON, D.C. 20362
    01CY ATTN CAPT R. PITKIN

COMMANDER
NAVAL SPACE SURVEILLANCE SYSTEM
DAHLGREN, VA 22448
    01CY ATTN CAPT J. H. BURTON

OFFICER-IN-CHARGE
NAVAL SURFACE WEAPONS CENTER
WHITE OAK, SILVER SPRING, MD 20910
    01CY ATTN CODE F31

DIRECTOR
STRATEGIC SYSTEMS PROJECT OFFICE
DEPARTMENT OF THE NAVY
WASHINGTON, D.C. 20376
    01CY ATTN NSP-2141
    01CY ATTN NSSP-2722 FRED WIMBERLY

NAVAL SPACE SYSTEM ACTIVITY
P. O. BOX 92960
WORLDWAY POSTAL CENTER
LOS ANGELES, CALIF. 90009
    01CY ATTN A. B. HAZZARD

COMMANDER
NAVAL SURFACE WEAPONS CENTER
DAHLGREN LABORATORY
DAHLGREN, VA 22448
    01CY ATTN CODE DF-14 R. BUTLER

COMMANDING OFFICER
NAVY SPACE SYSTEMS ACTIVITY
P.O. BOX 92960
WORLDWAY POSTAL CENTER
LOS ANGELES, CA. 90009
    01CY ATTN CODE 52

OFFICE OF NAVAL RESEARCH
ARLINGTON, VA 22217
    01CY ATTN CODE 465
    01CY ATTN CODE 461
    01CY ATTN CODE 402
    01CY ATTN CODE 420
    01CY ATTN CODE 421

COMMANDER
AEROSPACE DEFENSE COMMAND/DC
DEPARTMENT OF THE AIR FORCE
ENT AFB, CO 80912
    01CY ATTN DC MR. LONG

COMMANDER
AEROSPACE DEFENSE COMMAND/XPD
DEPARTMENT OF THE AIR FORCE
ENT AFB, CO 80912
    01CY ATTN XPDQQ
    01CY ATTN XP

AIR FORCE GEOPHYSICS LABORATORY
HANSCOM AFB, MA 01731
    01CY ATTN OPR HAROLD GARDNER
    01CY ATTN OPR-1 JAMES C. ULWICK
    01CY ATTN LKB KENNETH S. W. CHAMPION
    01CY ATTN OPR ALVA T. STAIR
    01CY ATTN PHP JULES AARONS
    01CY ATTN PHD JURGEN BUCHAU
    01CY ATTN PHD JOHN P. MULLEN

AF WEAPONS LABORATORY
KIRTLAND AFB, NM 87117
    01CY ATTN SUL
    01CY ATTN CA ARTHUR H. GUENTHER
    01CY ATTN DYC CAPT J. BARRY
    01CY ATTN DYC JOHN M. KAMM
    01CY ATTN DYT CAPT MARK A. FRY
    01CY ATTN DES MAJ GARY GANONG
    01CY ATTN DYC J. JANNI

AFTAC
PATRICK AFB, FL 32925
    01CY   ATTN TF/MAJ WILEY
    01CY   ATTN TN

AIR FORCE AVIONICS LABORATORY
WRIGHT-PATTERSON AFB, OH 45433
    01CY   ATTN AAD   WADE HUNT
    01CY   ATTN AAD   ALLEN JOHNSON

DEPUTY CHIEF OF STAFF
RESEARCH, DEVELOPMENT, & ACQ
DEPARTMENT OF THE AIR FORCE
WASHINGTON, D.C. 20330
    01CY   ATTN AFRDQ

HEADQUARTERS
ELECTRONIC SYSTEMS DIVISION/XR
DEPARTMENT OF THE AIR FORCE
HANSCOM AFB, MA 01731
    01CY   ATTN XR   J. DEAS

HEADQUARTERS
ELECTRONIC SYSTEMS DIVISION/YSEA
DEPARTMENT OF THE AIR FORCE
HANSCOM AFB, MA 01731
    01CY   ATTN YSEA

HEADQUARTERS
ELECTRONIC SYSTEMS DIVISION/DC
DEPARTMENT OF THE AIR FORCE
HANSCOM AFB, MA 01731
    01CY   ATTN DCKC   MAJ J. C. CLARK

HEADQUARTERS
ELECTRONIC SYSTEMS DIVISION, AFSC
HANSCOM AFB, MA 01731
    01CY   ATTN XRW
    01CY   ATTN JAMES WHELAN

COMMANDER
FOREIGN TECHNOLOGY DIVISION, AFSC
WRIGHT-PATTERSON AFB, OH 45433
    01CY   ATTN NICD   LIBRARY
    01CY   ATTN ETDP   B. BALLARD

COMMANDER
ROME AIR DEVELOPMENT CENTER, AFSC
GRIFFISS AFB, NY 13441
    01CY   ATTN DOC LIBRARY/TSLD
    01CY   ATTN OCSE   V. COYNE

SAMSO/SZ
POST OFFICE BOX 92960
WORLDWAY POSTAL CENTER
LOS ANGELES, CA 90009
(SPACE DEFENSE SYSTEMS)
    01CY ATTN SZJ

STRATEGIC AIR COMMAND/XPFS
OFFUTT AFB, NB 68113
    01CY ATTN XPFS MAJ B. STEPHAN
    01CY ATTN ADWATE MAJ BRUCE BAUER
    01CY ATTN NRT
    01CY ATTN DOK CHIEF SCIENTIST

SAMSO/YA
P. O. BOX 92960
WORLDWAY POSTAL CENTER
LOS ANGELES, CA 90009
    01CY ATTN YAT CAPT L. BLACKWELDER

SAMSO/SK
P. O. BOX 92960
WORLDWAY POSTAL CENTER
LOS ANGELES, CA 90009
    01CY ATTN SKA (SPACE COMM SYSTEMS) M. CLAVIN

SAMSO/MN
NORTON AFB, CA 92409
(MINUTEMAN)
    01CY ATTN MNNL LTC KENNEDY

COMMANDER
ROME AIR DEVELOPMENT CENTER, AFSC
HANSCOM AFB, MA 01731
    01CY ATTN EEP A. LORENTZEN

DEPARTMENT OF ENERGY

DEPARTMENT OF ENERGY
ALBUQUERQUE OPERATIONS OFFICE
P. O. BOX 5400
ALBUQUERQUE, NM 87115
    01CY ATTN DOC CON FOR D. SHERWOOD

DEPARTMENT OF ENERGY
LIBRARY ROOM G-042
WASHINGTON, D.C. 20545
    01CY ATTN DOC CON FOR A. LABOWITZ

EG&G, INC.
LOS ALAMOS DIVISION
P. O. BOX 809
LOS ALAMOS, NM 85544
    01CY ATTN DOC CON FOR J. BREEDLOVE

UNIVERSITY OF CALIFORNIA
LAWRENCE LIVERMORE LABORATORY
P. O. BOX 808
LIVERMORE, CA 94550
    01CY ATTN DOC CON FOR TECH INFO DEPT
    01CY ATTN DOC CON FOR L-389 R. OTT
    01CY ATTN DOC CON FOR L-31 R. HAGER
    01CY ATTN DOC CON FOR L-46 F. SEWARD

LOS ALAMOS SCIENTIFIC LABORATORY
P. O. BOX 1663
LOS ALAMOS, NM 87545
    01CY ATTN DOC CON FOR J. WOLCOTT
    01CY ATTN DOC CON FOR R. F. TASCHEK
    01CY ATTN DOC CON FOR E. JONES
    01CY ATTN DOC CON FOR J. MALIK
    01CY ATTN DOC CON FOR R. JEFFRIES
    01CY ATTN DOC CON FOR J. ZINN
    01CY ATTN DOC CON FOR P. KEATON
    01CY ATTN DOC CON FOR D. WESTERVELT

SANDIA LABORATORIES
P. O. BOX 5800
ALBUQUERQUE, NM 87115
    01CY ATTN DOC CON FOR J. MARTIN
    01CY ATTN DOC CON FOR W. BROWN
    01CY ATTN DOC CON FOR A. THORNBROUGH
    01CY ATTN DOC CON FOR T. WRIGHT
    01CY ATTN DOC CON FOR D. DAHLGREN
    01CY ATTN DOC CON FOR 3141
    01CY ATTN DOC CON FOR SPACE PROJECT DIV

OTHER GOVERNMENT

CENTRAL INTELLIGENCE AGENCY
ATTN RD/SI, RM 5G48, HQ BLDG
WASHINGTON, D.C. 20505
    01CY ATTN OSI/PSID RM 5F 19

DEPARTMENT OF COMMERCE
NATIONAL BUREAU OF STANDARDS
WASHINGTON, D.C. 20234
    (ALL CORRES: ATTN SEC OFFICER FOR)
    01CY ATTN R. MOORE

DEPARTMENT OF TRANSPORTATION
OFFICE OF THE SECRETARY
TAD-44.1, ROOM 10402-B
400 7TH STREET, S.W.
WASHINGTON, D.C. 20590
    01CY ATTN R. LEWIS
    01CY ATTN R. DOHERTY

INSTITUTE FOR TELECOM SCIENCES
NATIONAL TELECOMMUNICATIONS & INFO ADMIN
BOULDER, CO 80303
    01CY ATTN A. JEAN (UNCLASS ONLY)
    01CY ATTN W. UTLAUT
    01CY ATTN D. CROMBIE
    01CY ATTN L. BERRY

NATIONAL OCEANIC & ATMOSPHERIC ADMIN
ENVIRONMENTAL RESEARCH LABORATORIES
DEPARTMENT OF COMMERCE
BOULDER, CO 80302
    01CY ATTN R. GRUBB
    01CY ATTN AERONOMY LAB G. REID

NASA
GODDARD SPACE FLIGHT CENTER
GREENBELT, MD 20771
    01CY ATTN P. CORRIGAN

DEPARTMENT OF DEFENSE CONTRACTORS

AEROSPACE CORPORATION
P. O. BOX 92957
LOS ANGELES, CA 90009
    01CY   ATTN I. GARFUNKEL
    01CY   ATTN T. SALMI
    01CY   ATTN V. JOSEPHSON
    01CY   ATTN S. BOWER
    01CY   ATTN N. STOCKWELL
    01CY   ATTN D. OLSEN
    01CY   ATTN J. CARTER
    01CY   ATTN F. MORSE
    01CY   ATTN SMFA FOR PWW

ANALYTICAL SYSTEMS ENGINEERING CORP
5 OLD CONCORD ROAD
BURLINGTON, MA 01803
    01CY   ATTN RADIO SCIENCES

BERKELEY RESEARCH ASSOCIATES, INC.
P. O. BOX 983
BERKELEY, CA 94701
    01CY   ATTN J. WORKMAN

BOEING COMPANY, THE
P. O. BOX 3707
SEATTLE, WA 98124
    01CY   ATTN G. KEISTER
    01CY   ATTN D. MURRAY
    01CY   ATTN G. HALL
    01CY   ATTN J. KENNEY

CALIFORNIA AT SAN DIEGO, UNIV OF
IPAPS, B-019
LA JOLLA, CA 92093
    01CY   ATTN HENRY G. BOOKER

BROWN ENGINEERING COMPANY, INC.
CUMMINGS RESEARCH PARK
HUNTSVILLE, AL 35807
    01CY   ATTN ROMEO A. DELIBERIS

CHARLES STARK DRAPER LABORATORY, INC.
555 TECHNOLOGY SQUARE
CAMBRIDGE, MA 02139
    01CY   ATTN D. B. COX
    01CY   ATTN J. P. GILMORE

COMPUTER SCIENCES CORPORATION
6565 ARLINGTON BLVD
FALLS CHURCH, VA 22046
    01CY   ATTN H. BLANK
    01CY   ATTN JOHN SPOOR
    01CY   ATTN C. NAIL

COMSAT LABORATORIES
LINTHICUM ROAD
CLARKSBURG, MD 20734
    01CY ATTN G. HYDE

CORNELL UNIVERSITY
DEPARTMENT OF ELECTRICAL ENGINEERING
ITHACA, NY 14850
    01CY ATTN D. T. FARLEY JR

ELECTROSPACE SYSTEMS, INC.
BOX 1359
RICHARDSON, TX 75080
    01CY ATTN H. LOGSTON
    01CY ATTN SECURITY (PAUL PHILLIPS)

ESL INC.
495 JAVA DRIVE
SUNNYVALE, CA 94086
    01CY ATTN J. ROBERTS
    01CY ATTN JAMES MARSHALL
    01CY ATTN C. W. PRETTIE

FORD AEROSPACE & COMMUNICATIONS CORP
3939 FABIAN WAY
PALO ALTO, CA 94303
    01CY ATTN J. T. MATTINGLEY

GENERAL ELECTRIC COMPANY
SPACE DIVISION
VALLEY FORGE SPACE CENTER
GODDARD BLVD KING OF PRUSSIA
P. O. BOX 8555
PHILADELPHIA, PA 19101
    01CY ATTN M. H. BORTNER SPACE SCI LAB

GENERAL ELECTRIC COMPANY
P. O. BOX 1122
SYRACUSE, NY 13201
    01CY ATTN F. REIBERT

GENERAL ELECTRIC COMPANY
TEMPO-CENTER FOR ADVANCED STUDIES
816 STATE STREET (P.O. DRAWER QQ)
SANTA BARBARA, CA 93102
    01CY ATTN DASIAC
    01CY ATTN DON CHANDLER
    01CY ATTN TOM BARRETT
    01CY ATTN TIM STEPHANS
    01CY ATTN WARREN S. KNAPP
    01CY ATTN WILLIAM MCNAMARA
    01CY ATTN B. GAMBILL
    01CY ATTN MACK STANTON

GENERAL ELECTRIC TECH SERVICES CO., INC.
HMES
COURT STREET
SYRACUSE, NY 13201
    01CY ATTN G. MILLMAN

GENERAL RESEARCH CORPORATION
SANTA BARBARA DIVISION
P. O. BOX 6770
SANTA BARBARA, CA 93111
    01CY ATTN JOHN ISE JR
    01CY ATTN JOEL GARBARINO

GEOPHYSICAL INSTITUTE
UNIVERSITY OF ALASKA
FAIRBANKS, AK 99701
      (ALL CLASS ATTN: SECURITY OFFICER)
    01CY ATTN T. N. DAVIS (UNCL ONLY)
    01CY ATTN NEAL BROWN (UNCL ONLY)
    01CY ATTN TECHNICAL LIBRARY

GTE SYLVANIA, INC.
ELECTRONICS SYSTEMS GRP-EASTERN DIV
77 A STREET
NEEDHAM, MA 02194
    01CY ATTN MARSHAL CROSS

ILLINOIS, UNIVERSITY OF
DEPARTMENT OF ELECTRICAL ENGINEERING
URBANA, IL 61803
    01CY ATTN K. YEH

ILLINOIS, UNIVERSITY OF
107 COBLE HALL
801 S. WRIGHT STREET
URBANA, IL 60680
    (ALL CORRES ATTN SECURITY SUPERVISOR FOR)
    01CY ATTN K. YEH

INSTITUTE FOR DEFENSE ANALYSES
400 ARMY-NAVY DRIVE
ARLINGTON, VA 22202
    01CY ATTN J. M. AEIN
    01CY ATTN ERNEST BAUER
    01CY ATTN HANS WOLFHARD
    01CY ATTN JOEL BENGSTON

HSS, INC.
2 ALFRED CIRCLE
BEDFORD, MA 01730
    01CY ATTN DONALD HANSEN

INTL TEL & TELEGRAPH CORPORATION
500 WASHINGTON AVENUE
NUTLEY, NJ 07110
    01CY ATTN TECHNICAL LIBRARY

JAYCOR
1401 CAMINO DEL MAR
DEL MAR, CA 92014
    01CY ATTN S. R. GOLDMAN

JOHNS HOPKINS UNIVERSITY
APPLIED PHYSICS LABORATORY
JOHNS HOPKINS ROAD
LAUREL, MD 20810
 01CY ATTN DOCUMENT LIBRARIAN
 01CY ATTN THOMAS POTEMRA
 01CY ATTN JOHN DASSOULAS

LOCKHEED MISSILES & SPACE CO INC
P. O. BOX 504
SUNNYVALE, CA 94088
 01CY ATTN DEPT 60-12
 01CY ATTN D. R. CHURCHILL

LOCKHEED MISSILES AND SPACE CO INC
3251 HANOVER STREET
PALO ALTO, CA 94304
 01CY ATTN MARTIN WALT DEPT 52-10
 01CY ATTN RICHARD G. JOHNSON DEPT 52-12
 01CY ATTN W. L. IMHOF DEPT 52-12

KAMAN SCIENCES CORP
P. O. BOX 7463
COLORADO SPRINGS, CO 80933
 01CY ATTN T. MEAGHER

LINKABIT CORP
10453 ROSELLE
SAN DIEGO, CA 92121
 01CY ATTN IRWIN JACOBS

LOWELL RSCH FOUNDATION, UNIVERSITY OF
450 AIKEN STREET
LOWELL, MA 01854
 01CY ATTN K. BIBL

M.I.T. LINCOLN LABORATORY
P. O. BOX 73
LEXINGTON, MA 02173
 01CY ATTN DAVID M. TOWLE
 01CY ATTN P. WALDRON
 01CY ATTN L. LOUGHLIN
 01CY ATTN D. CLARK

MARTIN MARIETTA CORP
ORLANDO DIVISION
P. O. BOX 5837
ORLANDO, FL 32805
 01CY ATTN R. HEFFNER

MCDONNELL DOUGLAS CORPORATION
5301 BOLSA AVENUE
HUNTINGTON BEACH, CA 92647
 01CY ATTN N. HARRIS
 01CY ATTN J. MOULE
 01CY ATTN GEORGE MROZ
 01CY ATTN W. OLSON
 01CY ATTN R. W. HALPRIN
 01CY ATTN TECHNICAL LIBRARY SERVICES

MISSION RESEARCH CORPORATION
735 STATE STREET
SANTA BARBARA, CA 93101
    01CY   ATTN P. FISCHER
    01CY   ATTN W. F. CREVIER
    01CY   ATTN STEVEN L. GUTSCHE
    01CY   ATTN D. SAPPENFIELD
    01CY   ATTN R. BOGUSCH
    01CY   ATTN R. HENDRICK
    01CY   ATTN RALPH KILB
    01CY   ATTN DAVE SOWLE
    01CY   ATTN F. FAJEN
    01CY   ATTN M. SCHEIBE
    01CY   ATTN CONRAD L. LONGMIRE
    01CY   ATTN WARREN A. SCHLUETER

MITRE CORPORATION, THE
P. O. BOX 208
BEDFORD, MA 01730
    01CY   ATTN JOHN MORGANSTERN
    01CY   ATTN G. HARDING
    01CY   ATTN C. E. CALLAHAN

MITRE CORP
WESTGATE RESEARCH PARK
1820 DOLLY MADISON BLVD
MCLEAN, VA 22101
    01CY   ATTN W. HALL
    01CY   ATTN W. FOSTER

PACIFIC-SIERRA RESEARCH CORP
1456 CLOVERFIELD BLVD.
SANTA MONICA, CA 90404
    01CY   ATTN E. C. FIELD JR

PENNSYLVANIA STATE UNIVERSITY
IONOSPHERE RESEARCH LAB
318 ELECTRICAL ENGINEERING EAST
UNIVERSITY PARK, PA 16802
    (NO CLASSIFIED TO THIS ADDRESS)
    01CY   ATTN IONOSPHERIC RESEARCH LAB

PHOTOMETRICS, INC.
442 MARRETT ROAD
LEXINGTON, MA 02173
    01CY   ATTN IRVING L. KOFSKY

PHYSICAL DYNAMICS INC.
P. O. BOX 3027
BELLEVUE, WA 98009
    01CY   ATTN E. J. FREMOUW

PHYSICAL DYNAMICS INC.
P. O. BOX 1069
BERKELEY, CA 94701
    01CY   ATTN A. THOMPSON

17

R & D ASSOCIATES
P. O. BOX 9695
MARINA DEL REY, CA 90291
    01CY ATTN FORREST GILMORE
    01CY ATTN BRYAN GABBARD
    01CY ATTN WILLIAM B. WRIGHT JR
    01CY ATTN ROBERT F. LELEVIER
    01CY ATTN WILLIAM J. KARZAS
    01CY ATTN H. ORY
    01CY ATTN C. MACDONALD
    01CY ATTN R. TURCO

RAND CORPORATION, THE
1700 MAIN STREET
SANTA MONICA, CA 90406
    01CY ATTN CULLEN CRAIN
    01CY ATTN ED BEDROZIAN

RIVERSIDE RESEARCH INSTITUTE
80 WEST END AVENUE
NEW YORK, NY 10023
    01CY ATTN VINCE TRAPANI

SCIENCE APPLICATIONS, INC.
P. O. BOX 2351
LA JOLLA, CA 92038
    01CY ATTN LEWIS M. LINSON
    01CY ATTN DANIEL A. HAMLIN
    01CY ATTN D. SACHS
    01CY ATTN E. A. STRAKER
    01CY ATTN CURTIS A. SMITH
    01CY ATTN JACK MCDOUGALL

RAYTHEON CO.
528 BOSTON POST ROAD
SUDBURY, MA 01776
    01CY ATTN BARBARA ADAMS

SCIENCE APPLICATIONS, INC.
HUNTSVILLE DIVISION
2109 W. CLINTON AVENUE
SUITE 700
HUNTSVILLE, AL 35805
    01CY ATTN DALE H. DIVIS

SCIENCE APPLICATIONS, INCORPORATED
8400 WESTPARK DRIVE
MCLEAN, VA 22101
    01CY ATTN J. COCKAYNE

SCIENCE APPLICATIONS, INC.
80 MISSION DRIVE
PLEASANTON, CA 94566
    01CY ATTN SZ

SRI INTERNATIONAL
333 RAVENSWOOD AVENUE
MENLO PARK, CA 94025
    01CY   ATTN DONALD NEILSON
    01CY   ATTN ALAN BURNS
    01CY   ATTN G. SMITH
    01CY   ATTN L. L. COBB
    01CY   ATTN DAVID A. JOHNSON
    01CY   ATTN WALTER G. CHESNUT
    01CY   ATTN CHARLES L. RINO
    01CY   ATTN WALTER JAYE
    01CY   ATTN M. BARON
    01CY   ATTN RAY L. LEADABRAND
    01CY   ATTN G. CARPENTER
    01CY   ATTN G. PRICE
    01CY   ATTN J. PETERSON
    01CY   ATTN R. HAKE, JR.
    01CY   ATTN V. GONZALES
    01CY   ATTN D. MCDANIEL

TECHNOLOGY INTERNATIONAL CORP
75 WIGGINS AVENUE
BEDFORD, MA 01730
    01CY   ATTN W. P. BOQUIST

TRW DEFENSE & SPACE SYS GROUP
ONE SPACE PARK
REDONDO BEACH, CA 90278
    01CY   ATTN R. K. PLEBUCH
    01CY   ATTN S. ALTSCHULER
    01CY   ATTN D. DEE

VISIDYNE, INC.
19 THIRD AVENUE
NORTH WEST INDUSTRIAL PARK
BURLINGTON, MA 01803
    01CY   ATTN CHARLES HUMPHREY
    01CY   ATTN J. W. CARPENTER

IONOSPHERIC MODELING DISTRIBUTION LIST
UNCLASSIFIED ONLY

PLEASE DISTRIBUTE ONE COPY TO EACH OF THE FOLLOWING PEOPLE:

ADVANCED RESEARCH PROJECTS AGENCY (ARPA)
STRATEGIC TECHNOLOGY OFFICE
ARLINGTON, VIRGINIA

    CAPT. DONALD M. LEVINE

NAVAL RESEARCH LABORATORY
WASHINGTON, D.C. 20375

    DR. P. MANGE
    DR. R. MEIER
    DR. E. SZUSZCZEWICZ - CODE 7127
    DR. TIMOTHY COFFEY - CODE 6700
    DR. S. OSSAKOW - CODE 6780
    DR. J. GOODMAN - CODE 7560

SCIENCE APPLICATIONS, INC.
1250 PROSPECT PLAZA
LA JOLLA, CALIFORNIA 92037

    DR. D. A. HAMLIN
    DR. L. LINSON
    DR. D. SACHS

DIRECTOR OF SPACE AND ENVIRONMENTAL LABORATORY
NOAA
BOULDER, COLORADO 80302

    DR. A. GLENN JEAN
    DR. G. W. ADAMS
    DR. D. N. ANDERSON
    DR. K. DAVIES
    DR. R. F. DONNELLY

A. F. GEOPHYSICS LABORATORY
L. G. HANSOM FIELD
BEDFORD, MASS. 01730

    DR. T. ELKINS
    DR. W. SWIDER
    MRS. R. SAGALYN
    DR. J. M. FORBES
    DR. T. J. KENESHEA
    DR. J. AARONS

20

OFFICE OF NAVAL RESEARCH
800 NORTH QUINCY STREET
ARLINGTON, VIRGINIA 22217

    DR. H. MULLANEY

COMMANDER
NAVAL ELECTRONICS LABORATORY CENTER
SAN DIEGO, CALIFORNIA 92152

    DR. M. BLEIWEISS
    DR. I. ROTHMULLER
    DR. V. HILDEBRAND
    MR. R. ROSE

U. S. ARMY ABERDEEN RESEARCH AND DEVELOPMENT CENTER
BALLISTIC RESEARCH LABORATORY
ABERDEEN, MARYLAND

    DR. J. HEIMERL

COMMANDER
NAVAL AIR SYSTEMS COMMAND
DEPARTMENT OF THE NAVY
WASHINGTON, D.C. 20360

    DR. T. CZUBA

HARVARD UNIVERSITY
HARVARD SQUARE
CAMBRIDGE, MASS. 02138

    DR. M. B. MCELROY
    DR. R. LINDZEN

PENNSYLVANIA STATE UNIVERSITY
UNIVERSITY PARK, PENNSYLVANIA 16802

    DR. J. S. NISBET
    DR. P. R. ROHRBAUGH
    DR. D. E. BARAN
    DR. L. A. CARPENTER
    DR. M. LEE
    DR. R. DIVANY
    DR. P. BENNETT
    DR. E. KLEVANS

UNIVERSITY OF CALIFORNIA, LOS ANGELES
405 HILLGARD AVENUE
LOS ANGELES, CALIFORNIA 90024

    DR. F. V. CORONITI
    DR. C. KENNEL

UNIVERSITY OF CALIFORNIA, BERKELEY
BERKELEY, CALIFORNIA 94720

    DR. M. HUDSON

UTAH STATE UNIVERSITY
4TH N. AND 8TH STREETS
LOGAN, UTAH 84322

    DR. P. M. BANKS
    DR. R. HARRIS
    DR. V. PETERSON
    DR. R. MEGILL
    DR. K. BAKER

CORNELL UNIVERSITY
ITHACA, NEW YORK 14850

    DR. W. E. SWARTZ
    DR. R. SUDAN
    DR. D. FARLEY
    DR. M. KELLEY
    DR. E. OTT

NASA
GODDARD SPACE FLIGHT CENTER
GREENBELT, MARYLAND 20771

    DR. S. CHANDRA
    DR. K. MAEDO

PRINCETON UNIVERSITY
PLASMA PHYSICS LABORATORY
PRINCETON, NEW JERSEY 08540

    DR. F. PERKINS
    DR. E. FRIEMAN

INSTITUTE FOR DEFENSE ANALYSIS
400 ARMY/NAVY DRIVE
ARLINGTON, VIRGINIA 22202

    DR. E. BAUER

22

UNIVERSITY OF PITTSBURGH
PITTSBURGH, PA. 15213

DR. N. ZABUSKY
DR. M. BIONDI